# An investigation of chlorine ligands in transition-metal complexes via $^{35}$Cl SSNMR and DFT calculations

Christopher A. O'Keefe,[a] Karen E. Johnston,[a] Kiplangat Sutter,[b] Jochen Autschbach,[b] Régis Gauvin,[c] Julien Trébosc,[c] Laurent Delevoye,[c] Nicolas Popoff,[d] Mostafa Taoufik,[d] Konstantin Oudatchin,[e] and Robert W. Schurko[a]*

[a] Department of Chemistry and Biochemistry, University of Windsor, Windsor, Ontario, N9B 3P4, Canada

[b] Department of Chemistry, University at Buffalo, State University of New York, Buffalo, NY 14260

[c]Université Lille Nord de France, CNRS UMR8181, Unité de Catalyse et de Chimie du Solide, UCCS USTL, F-59655 Villeneuve d'Ascq, France

[d]Laboratoire de Chimie, Catalyse, Polymères et Procédés (UMR-C2P2-5265 CNRS/ESCPE-Lyon/UCBL) ESCPE Lyon, F-308-43, Boulevard du 11 Novembre 1918, F-69616 Villeurbanne Cedex, France

[e]Steacie Institute for Molecular Sciences, National Research Council, 100 Sussex Drive, Ottawa, Ontario, K1A OR6, Canada

*Author to whom correspondence should be addressed

Phone: (519) 253-3000 x3548

Fax: (519) 973-7098

E-mail: rschurko@uwindsor.ca

**Abstract**

Chlorine ligands in a variety of diamagnetic transition-metal (TM) complexes in common structural motifs were studied using $^{35}$Cl solid-state NMR (SSNMR) and insight into the origin of the observed $^{35}$Cl NMR parameters was gained through first-principles density functional theory (DFT) calculations. The WURST-CPMG pulse sequence and the variable-offset cumulative spectrum (VOCS) methods were used to acquire static $^{35}$Cl SSNMR powder patterns at both standard (9.4 T) and ultra-high (21.1 T) magnetic field strengths, with the later affording higher signal-to-noise ratios (S/N) and reduced experimental times (i.e., < 1h). Analytical simulations were performed to extract the $^{35}$Cl electric field gradient (EFG) tensor and chemical shift (CS) tensor parameters. It was found that the chlorine ligands in various bonding environments (i.e., bridging, terminal-axial and terminal-equatorial) have drastically different $^{35}$Cl EFG tensor parameters, suggesting that $^{35}$Cl SSNMR is ideal for characterizing chlorine ligands in TM complexes. A detailed localized molecular orbital (LMO) analysis was completed for $NbCl_5$. It was found that the contributions of individual molecular orbitals must be considered to fully explain the observed EFG parameters, thereby negating simple arguments based on comparison of bond lengths and angles. Finally, we discuss the application of $^{35}$Cl SSNMR for the structural characterization of $WCl_6$ that has been grafted onto a silica support material. The resulting tungsten-chloride surface species is shown to be structurally distinct from the parent compound.

## Introduction

Group V and VI transition metals (TM) are commonly used to fabricate a wide range of complexes with various uses, such as reagents in redox reactions,[1–4] anti-tumour agents[5–7] and superconducting materials.[8–10] However, perhaps their most ubiquitous use is for the catalysis of reactions involving organic and organometallic species.[11–16] Their multiple oxidation states and relatively large atomic sizes allow for the coordination of a variety of ligands and the synthesis of catalysts that can be fine-tuned for specific purposes. Such complexes find use in both homogeneous and heterogeneous catalytic processes; the latter is widely thought to afford higher selectivity and efficiency.[17,18] As a result, the design and application of heterogeneous catalysts, which involves the chemical or physical immobilization of the TM species on high-surface area materials, represent burgeoning areas of research.[19–21]

Structural characterization of heterogeneous catalysts is often difficult, as the support materials are almost always disordered and insoluble, thereby limiting or preventing their analysis by conventional techniques such as X-ray diffraction (XRD) or solution-state NMR spectroscopy. Surface techniques such as X-ray photoelectron spectroscopy (XPS)[22] and IR spectroscopy[23,24] have previously been used to study immobilized species; however, the structural information is often limited. Solid-state NMR (SSNMR) spectroscopy is now widely used for molecular-level characterization of heterogeneous catalysts,[25–28] providing information on structural motifs, bonding, interatomic distances, symmetry and ground-state electronic distributions. Furthermore, unlike XRD methods, SSNMR is capable of probing short-range order in systems lacking long-range order (i.e., amorphous and/or disordered solids).

SSNMR experiments involving $^{1}$H and $^{13}$C are the most common for studies of heterogeneous catalysts.[27,29–31] However, our research group has shown that it may be possible to investigate such systems from the perspective of the TM nuclei; to date, we have characterized bulk metallocene complexes utilizing $^{91}$Zr, $^{47/49}$Ti, $^{93}$Nb and $^{139}$La SSNMR.[32–36] The spectra of many of these nuclei are very broad, ranging from several hundred kHz to MHz in breadth; accordingly, S/N tends to be very poor in many of these spectra, which suggests limitations for studying the diluted, supported TM species in heterogeneous catalysts. However, recent developments in broadband excitation sequences and other signal enhancing techniques,[37–39] along with the increasing availability of higher magnetic field strengths and improved NMR probes and hardware, suggest that SSNMR of such systems may hold much promise. Unfortunately, for certain TM nuclei such as $^{95/97}$Mo, $^{103}$Rh, $^{181}$Ta and $^{183}$W, probing the metal centre using SSNMR currently remains challenging due to their inherently unreceptive natures. In such cases, it is often more convenient and informative to conduct NMR experiments involving other nuclei on the ligands surrounding the metal centre, since their NMR parameters are likely to be sensitive to structural differences. A prime example of this is chlorine, which is found widely in many TM complexes.

Chlorine has two naturally occurring NMR-active isotopes, $^{35}$Cl and $^{37}$Cl, with natural abundances of 75.78 and 24.22%, respectively. Both have nuclear spins of $I = 3/2$ and low gyromagnetic ratios ("low-γ"), with relatively small quadrupole moments of −8.165 and −6.435 fm$^2$.[40] $^{35}$Cl is the preferred target NMR nuclide due to its higher receptivity (i.e., both its natural abundance and Larmor frequency are higher).

The $^{35}$Cl quadrupolar interaction (QI), which arises from coupling between the $^{35}$Cl nuclear quadrupole moment and local electric field gradients (EFGs) at the $^{35}$Cl nucleus, is very sensitive to subtle differences in structure. Accordingly, the quadrupolar coupling constant, $C_Q$, and the asymmetry parameter, $\eta_Q$ (see **Table 1** for definitions), which are determined from simulations of the $^{35}$Cl SSNMR powder patterns, reflect variance in structure and bonding. $^{35}$Cl SSNMR spectra typically exhibit central transition (CT, +1/2↔–1/2) powder patterns that are strongly influenced by the second-order quadrupolar interaction (SOQI); the two satellite transition patterns (ST, ±3/2↔±1/2) are predominantly broadened by the first-order quadrupolar interaction (FOQI), and are rarely observed in $^{35}$Cl SSNMR spectra (excepting in cases where the magnitude of $C_Q$ is very small).

The majority of $^{35}$Cl SSNMR studies to date have focused on systems with the chlorine atoms at the centre of ground-state electronic distributions of high spherical or Platonic symmetry (e.g., $Cl^-$ ions weakly coordinated by water molecules and other ligands, $ClO_4^-$, etc.). Such environments are generally associated with small values of $C_Q$ and have relatively narrow $^{35}$Cl CT powder patterns that can be acquired using conventional Hahn-echo experiments and high-power rectangular pulses.[41–44] Examples of such systems include metal-chloride salts, hydrochloride (HCl) salts of amino acids and pharmaceuticals. The application of $^{35}$Cl SSNMR to systems in which Cl is involved in covalent bonding is very rare by comparison, since the values of $C_Q$ are much larger and the powder patterns much broader. Some recent works include investigations of group 13 chloride salts,[45] chlorine-containing metallocenes,[46] organometallic transition metal complexes[47] and organic compounds with covalent C-Cl bonds.[48] All of these

studies report the use of high magnetic fields and specialized pulse sequences due to the exceptionally broad $^{35}$Cl powder patterns associated with these systems. Such spectra, and the concomitant experiments necessary for their acquisition, fall under the classification of ultra-wideline (UW) NMR spectroscopy.[49,50]

Herein, we describe the application of $^{35}$Cl SSNMR in conjunction with first-principles density functional theory (DFT) calculations to study diamagnetic inorganic chlorine-containing TM complexes (**Scheme 1**) that exhibit a variety of common structural motifs and are representative of several broader classes of TM complexes widely used in catalysis. All of these compounds have been previously characterized by $^{35}$Cl NQR spectroscopy; this allows us to determine whether the values of $C_Q$ extracted from simple analytical simulations under the high-field approximation (i.e., $\nu_0 > \nu_Q$) are valid, and to also accurately measure the values of $\eta_Q$, which are unavailable from NQR spectra of spin-3/2 nuclides. First, we demonstrate the application of the Wideband Uniform-Rate Smooth Truncation-Quadrupolar Carr-Purcell-Meiboom-Gill (WURST-CPMG) pulse sequence[38,51] for the rapid acquisition (i.e., < 1h) of UW $^{35}$Cl SSNMR spectra at both 9.4 and 21.1 T. In one case, the use of $^{35}$Cl NMR and $^{35}$Cl NQR experiments in tandem for the differentiation of polymorphs is explored. Second, quadrupolar parameters determined from simulations of these spectra are compared to those obtained from plane wave DFT calculations. This data, along with theoretically derived $^{35}$Cl EFG tensor orientations, are used to propose relationships between the $^{35}$Cl quadrupolar parameters and the nature of the chlorine structural environments (i.e., the identity of the metal (M), M-Cl bond lengths, geometric arrangements, etc.). Third, a full analysis of the contributions of the individual molecular orbitals to the principal

components of the $^{35}Cl$ EFG tensor for $NbCl_5$ is presented, and utilized to explore the origins of the experimentally observed $^{35}Cl$ quadrupolar parameters. Fourth, we present an example of an application of $^{35}Cl$ SSNMR to a tungsten chloride species grafted onto a silica support material. Based on experimental and theoretical data on the bulk species presented herein, it is possible to make a rough structural interpretation of this result. Finally, we discuss the potential applications of this methodology for the study of heterogeneous TM chloride catalysts.

**Experimental and Computation Details**

*Sample Preparation.* Compounds α-$WCl_6$, $NbCl_5$, and $TaCl_5$ were purchased from Strem Chemicals and compounds $WOCl_4$, $MoOCl_4$, and $MoCl_5$ were purchased from Sigma-Aldrich Canada, Ltd. All samples were used without further purification or modification (phase purity was checked with powder XRD, *vide infra*). β-$WCl_6$ was prepared by the slow sublimation of the α-form under a nitrogen environment.[52] All of the compounds were stored and packed under an inert nitrogen atmosphere in a dry glove box due to their air- and moisture-sensitive natures. All samples were finely ground and packed into shortened 5 mm outer diameter glass NMR tubes, then capped and sealed with Parafilm to limit their exposure to atmosphere for the duration of the experiments.

*Preparation of $WCl_6$-$SiO_2$.* A toluene solution of $WCl_6$ was added to a toluene suspension of dehydroxylated silica (Degussa Aerosil 250, pretreated at 700°C under $10^{-5}$ bar vacuum) and the resulting mixture was stirred overnight at room temperature. After filtration of the supernatant, the solid was washed three times with toluene, one time with pentane and dried under vacuum ($10^{-5}$ bar). W w%: 5.48%. HCl evolution was checked by IR spectroscopy as in a previous communication.[53]

*Powder X-ray Diffraction (PXRD).* PXRD experiments were performed at 100 K on a Bruker Apex 2 Kappa Diffractometer using graphite monochromatized Mo $K_\alpha$ radiation ($\lambda$ = 0.7107 Å). Theoretical PXRD patterns were simulated for all samples using the Powder Cell software package.[54]

*$^{35}$Cl SSNMR Spectroscopy.* A Varian Infinity Plus Spectrometer equipped with a wide-bore Oxford 9.4 T magnet ($\nu_0(^1H)$ = 400 MHz and $\nu_0(^{35}Cl)$ = 39.16 MHz) was used for the acquisition of static (i.e., stationary samples) $^{35}$Cl SSNMR spectra for all samples. The experiments were conducted on a Varian Chemagnetics 5 mm triple-resonance (HXY) T3 MAS NMR probe. Spectra were also collected using a Bruker Avance II spectrometer with a 21.1 T ($\nu_0(^{35}Cl)$ = 88.2 MHz) standard-bore magnet at the National Ultrahigh-field NMR Facility for Solids in Ottawa, Ontario, Canada. A home-built 4 mm double resonance probe was used for all experiments. The spectrum of $WCl_6$-$SiO_2$ was acquired on a Bruker Avance III spectrometer with an 18.8 T standard-bore magnet using a 3.2 mm HX MAS probe at Université Lille Nord de France. Chemical shifts were referenced to 1 M NaCl (aq), with NaCl(s) ($\delta_{iso}$ = 0 ppm) used as a secondary reference.

All $^{35}$Cl CT powder patterns were too broad to be uniformly excited with a single, rectangular, high-power pulse. Hence, the WURST-CPMG pulse sequence[38,51] was used with a 50 μs WURST pulse swept over 2000 kHz (sweep rate of 40 MHz/ms) for experiments at 9.4 and 21.1 T whereas at 18.8 T, the WURST pulse was swept over 4000 kHz (sweep rate of 80 MHz/ms). The experiments at 18.8 T also used a continuous-wave $^1$H decoupling field of 30 kHz that was applied for the duration of the scan, including during the WURST pulses. A detailed list of the experimental parameters can be found

in the Supporting Information (**Tables S1-S3**). Spectra were acquired using the variable offset cumulative spectrum (VOCS) technique[55–57] with each sub-spectrum acquired using a transmitter offset of 100 kHz. Sub-spectra were processed using the NUTS program from Acorn software. The free induction decays (FIDs) of the sub-spectra were processed with digital filtering, Fourier transformation and a magnitude calculation. The individual sub-spectra were then co-added (9.4 T) or skyline projected (21.1 T) to produce the total spectrum. The spectra consist of a series of narrow lines, called *spikelets*, whose outer manifold is representative of the shape of the powder pattern. Analytical simulations of the spectra were generated using WSolids[58] (9.4 T) and QUEST[59] (21.1 T) software packages; precise values of the quadrupolar parameters are obtained by matching the positions of the key spectral discontinuities (i.e., "shoulders" and "horns"), and not the positions of the individual spikelets. Uncertainties in the quadrupolar parameters were estimated by bidirectional variation of each parameter, and visual comparison of experimental and simulated spectra.

$^{35}$Cl transverse relaxation time constants ($T_2$) were measured using the CPMG pulse sequence. Echo trains were acquired by placing the transmitter at each of the spectral discontinuities. The intensity of each echo train was then plotted as a function of time and fit to an exponential decay using the Origin software package.

*$^{35}$Cl NQR Spectroscopy.* Experiments were conducted on a Varian Chemagnetics triple resonance (HXY) T3 MAS probe with a 5 mm coil and a Varian Infinity Plus console. The probe was placed as far away from the magnet as possible to limit the effects from the external magnetic field. The Hahn-echo pulse sequence was used with a

3.5 μs 90° pulse width and a recycle delay of 0.5 s. Processing of the $^{35}$Cl NQR spectra was done using NUTS.

*Plane-Wave DFT Calculations.* $^{35}$Cl EFG and CS tensor parameters were calculated using the CASTEP[60] plane-wave density functional theory code in the Materials Studio 5.0 software package. Calculations employed the generalized gradient approximation (GGA), the gauge-including projector augmented wave (GIPAW) formalism and revised Perdew, Burke and Ernzerhof (rPBE) functionals, with the core-valence interactions being described by on-the-fly pseudopotentials (**Table S4**). Integrals over the Brillouin zone were performed using a Monkhorst-Pack grid with a *k*-point spacing of 0.07 Å$^{-1}$. Wavefunctions were expanded in plane waves with a kinetic energy cut-off of 300 eV. Crystal structures were obtained from the Inorganic Crystal Structure Database (ICSD) and calculations were completed both prior to and post geometry optimization of the structures (i.e., all of the atomic positions were allowed to vary simultaneously while the cell parameters were fixed). All calculations were performed on the Shared Hierarchical Academic Research Computing Network (SHARCNET) using either 8 or 16 cores and 16 GB of memory per core.

*$^{35}$Cl Natural Bond Orbital/Natural Local Molecular Orbital Analysis of $NbCl_5$.* All computations were performed using a developer's version of Amsterdam Density Functional (ADF)[61] package. Experimental single-crystal XRD crystal structures were used as starting structures for geometry optimization. For the computation of EFG tensor parameters and the geometry optimization routines, relativistic effects were included by utilizing the zeroth-order regular approximation (ZORA) in its scalar form.[62] All calculations were carried out using the revised Perdew-Burke-Ernzerhof (rPBE)

functional.[63,64] The triple-ζ doubly polarized (TZ2P) all-electron Slater-type basis sets were used for Nb and Cl in all computations. Localized Molecular Orbital (LMO) analyses of $^{35}$Cl EFGs were performed as described previously.[65] LMOs were generated using the natural bond orbital (NBO) algorithm[66] implemented in a locally modified version of the NBO 5.0 program.[67] The set of "natural" LMOs generated by the NBO code was used for the EFG analysis.

**Results and Discussion**

For ease of discussion, all complexes have been grouped according to their structural similarities (**Scheme 1**). Some of the complexes exist as *polymorphs* in the solid state, which are pure substances that crystallize in more than one stable phase, with each having a distinct arrangement of atoms.[68] Powder X-ray diffraction (pXRD) patterns, which are useful for determining the presence of known crystalline phases, as well as for detecting for the presence of multiple polymorphs and crystalline impurities, were acquired for all of the samples (see Supporting Information, **Figures S7-S11**).

Before each group of systems is discussed in detail, it is useful to comment on some of the common features observed for all of the $^{35}$Cl SSNMR spectra, as well as some of the aspects of the plane-wave DFT calculations of the $^{35}$Cl EFG tensor parameters. First, all $^{35}$Cl SSNMR spectra were acquired at both standard (9.4 T) and ultra-high magnetic field strengths (21.1 T). The higher field strength serves to increase S/N due to (*i*) a more favourable Boltzmann distribution and (*ii*) the reduction in the breadth of the SOQI-dominated CT pattern by an amount proportional to the inverse of $\boldsymbol{B}_0$. Despite the general superiority of the 21.1 T data in terms of increased S/N, reduced

experimental times and improved resolution, we note that the experiments completed at 9.4 T were crucial for parameterizing the experiments and optimizing our use of the 21.1 T spectrometer. The spectra acquired at 21.1 T are shown in the manuscript, while those acquired at 9.4 T are presented in the Supporting Information. The only exception to this was β-$WCl_6$, which was only studied at 9.4 T.

Second, the breadth of each powder pattern is extremely large (700 to 1750 kHz) due to broadening of the CT by the SOQI. For all of the systems discussed herein, the SOQI has a much larger effect on the CT powder pattern than the chlorine chemical shift anisotropy (CSA); hence, the spectral features arise almost solely from the former. As such, the values obtained for the isotropic chemical shift ($\delta_{iso}$), span ($\Omega$), skew ($\kappa$) and the Euler angles ($\alpha$, $\beta$ and $\gamma$) describing the relative orientations of the EFG and CS tensors (see **Table 1** for definitions) have large uncertainties associated with them. The chlorine CS tensor parameters were calculated and the results are shown in the Supporting Information, along with a figure demonstrating that the inclusion of CSA has little effect on the appearance of the powder patterns (**Table S7**, **Figure S17**).

Third, the extreme breadths of the CT powder patterns render it difficult to distinguish chlorine environments that are chemically similar (i.e., those with comparable bond lengths and angles) but crystallographically distinct. However, the specific types of bonding environment for chlorine (i.e., bridging, terminal-axial or terminal-equatorial) are easily discernable from the $^{35}$Cl SSNMR spectra. Furthermore, techniques such as $^{35}$Cl NQR and $T_2$ editing of CPMG echo trains generally allow for the resolution of chemically similar environments and the accurate measurement of the NMR parameters.

Fourth, higher intensity than expected is always observed in the higher frequency range (i.e., leftmost regions) of each spectrum in comparison to the low frequency (rightmost) range. This effect is more pronounced for certain samples in comparison to others probably due to effects such as $T_2$ anisotropy and/or variation in probe/circuit characteristics over the broad range of acquisition frequencies (*vide infra*). Fifth, in some cases, it is possible to acquire signal extending past the edges of the CT in each powder pattern. This signal is attributed to the $^{35}$Cl satellite transition (ST) patterns (i.e., $-3/2 \leftrightarrow -1/2$ and $+1/2 \leftrightarrow +3/2$), which are visible owing to the high abundance of chlorine in each complex. ST patterns are broadened immensely by the first-order quadrupolar interaction over a range of several MHz, and often are associated with $T_2(^{35}\text{Cl})$ parameters that are distinct from those of the CT. In the case of $^{35}$Cl, the ST patterns result in minimal interference with the CT patterns. We note that the acquisition of the full ST powder pattern is generally unnecessary for UW SSNMR spectra, since the CT pattern provides information on all of the relevant NMR parameters. However, with quadrupolar parameters obtained from simulations of the CT patterns, it is possible to rapidly locate the key discontinuities in the STs, and to potentially further refine the quadrupolar parameters.[57]

Despite the extreme breadths of the CT powder patterns, it was possible to attain high S/N, high-resolution spectra in relatively short time frames (e.g., 32 s to 26 min at 21.1 T) owing to the broadband excitation of the WURST pulses, the long $^{35}$Cl transverse relaxation times constants ($T_2$) that favour CPMG-type experiments and the high chlorine concentrations in these samples.

As mentioned, chlorine sites that are chemically very similar are not easily differentiated in the $^{35}$Cl SSNMR spectra, and therefore, analytical simulations are representative of the convolution of the quadrupolar parameters of these sites. By fitting the simulations to the positions of the well-defined discontinuities of the spectra, it was possible to extract the $^{35}$Cl EFG tensor parameters $C_Q$ and $\eta_Q$ (**Table 1**). $^{35}$Cl NQR measurements have previously been conducted on all of the samples discussed herein. Since NQR measurements on spin-3/2 nuclei involve the measurement of a single transition, no values of $\eta_Q$ are typically reported, which is a limitation of the NQR experiment.[69,70] Nonetheless, we see generally good agreement between our experimental values of $C_Q$ and those from NQR measurements on $^{35}$Cl nuclei possessing values of $\eta_Q$ near to zero (i.e., axially symmetric EFG tensors, **Table 2**).

The quadrupolar parameters determined from $^{35}$Cl NMR spectra, in conjunction with $^{35}$Cl EFG tensor parameters obtained from DFT calculations, were used to differentiate chlorine sites in distinct bonding arrangements (i.e., bridging ($Cl_{br}$), terminal-axial ($Cl_{ax}$) and terminal-equatorial ($Cl_{eq}$), *vide infra*). No consideration is given to the theoretical chlorine nuclear magnetic shielding tensors herein, since in most cases, the experimentally determined values of the chemical shift tensor parameters are associated with large uncertainties (as discussed above). The $^{35}$Cl EFG tensor parameters were calculated using CASTEP[60] both prior to and post-geometry optimization of each structure (**Table 2**). Geometry optimization of the structures resulted in small changes in bond lengths (**Table S5**), large changes in the computed EFG tensor parameters and greatly reduced forces between atoms (**Table S6**). In all cases, it was found that terminal chlorines have negative values of $C_Q$ whereas bridging chlorines have positive values.

The theoretical magnitudes of $C_Q$ are found to be consistently less than the experimentally measured values (**Figure 1**), similar to the observations of Rossini *et al.*[46] We note that the sign of $C_Q$ cannot be measured directly from the $^{35}$Cl NMR spectra, but is readily determined by the calculations.

*Tungsten(VI) chloride ($WCl_6$)*

Tungsten(VI) chloride exists as one of two polymorphs, α or β. The α form has one tungsten atom and one chlorine atom within the asymmetric unit (i.e., there is one unique chlorine environment). There are six chlorine atoms arranged around a central tungsten atom in an octahedral arrangement (**Scheme 1**). The β form has two tungsten atoms and three chlorine atoms within the asymmetric unit. The three chlorine sites have similar W–Cl bond lengths (2.23, 2.26 and 2.34 Å) and comparable Cl–W–Cl bond angles (91.3, 91.6 and 90.3°), resulting in a slightly distorted octahedral arrangement of chlorine atoms about the central tungsten atom.[71] Both forms feature hexagonal close packed lattices of chlorine atoms with tungsten ions filling the octahedral holes. The β form can be prepared from the α form by the slow sublimation of the α-form under $N_2$(g), or annealing a sample at a temperature greater than 200 °C (we chose the former procedure, see Experimental Section for details).[52]

The $^{35}$Cl static SSNMR spectra of α-$WCl_6$ and β-$WCl_6$ acquired at 21.1 T and 9.4 T, respectively, are shown in **Figure 2(A)** and **2(B)**. The latter compound was synthesized after experiments on all other samples had been conducted at 21.1 T; for reasons described below, no high-field data for this compound is presented. The CT of the α-form has a breadth of *ca.* 700 kHz and is characteristic of a powder pattern

broadened by the second-order quadrupolar interaction. The discontinuities typical of such a spectrum are clearly visible and the overall manifold of the spikelet pattern is representative of a single distinct chlorine site. This spectrum was best simulated with one site, $C_Q$ = 21.0 MHz and $\eta_Q$ = 0.029 (**Table 1**). This result is consistent with the α-form of tungsten(VI) chloride, which has one distinct chlorine environment. The CT of the β-form is ca. 1.5 MHz in breadth (due to the inverse dependence of the CT breadth on the applied external magnetic field strength). Despite the presence of multiple, magnetically and crystallographically distinct chlorine sites in the β-form, there appears to be only a single CT pattern, almost identical to the pattern acquired for α-$WCl_6$ at 9.4 T (**Figure S12**). In fact, this pattern can be subjected to a similar one-site simulation, yielding identical quadrupolar parameters to those of α-$WCl_6$ (within the limits of their uncertainties).

The benefit of ultra-wideline SSNMR experiments for rapidly acquiring spectra of anisotropically broadened powder patterns is tempered by their ability to resolve patterns arising from sites with very similar quadrupolar parameters. Even our attempts to acquire higher-resolution Hahn-echo spectra at key discontinuities failed to aid in clearly resolving the three unique chlorine sites in the β-form (**Figure 2 (C)**). In this case, $^{35}$Cl NQR is clearly very useful for trying to resolve the structurally similar sites in the β-form, as well as confirming the identity of each of these polymorphs. Both the α and β forms have previously been studied by $^{35}$Cl NQR spectroscopy. The $^{35}$Cl NQR spectrum of the α form has a single peak corresponding to a frequency at $\nu_Q^{NQR}$ = 10.520 MHz, whereas that of the β form has three peaks ($\nu_Q^{NQR}$ = 10.520, 10.525 and 10.576 MHz).[72] The values of $\nu_Q^{NQR}$ predicted from the experimentally determined $^{35}$Cl EFG tensor

parameters obtained for $WCl_6$ (**Table 2**), using the expression $\nu_Q^{NQR} = (C_Q/2)(1+(\eta_Q^2/3))^{1/2}$,[73] are in good agreement with the previously reported NQR frequencies. Using the same NMR probe, we conducted our own $^{35}Cl$ NQR experiments, and found a single peak at $\nu_Q^{NQR}$ = 10.5154 MHz for α-$WCl_6$ and three peaks at $\nu_Q^{NQR}$ = 10.512, 10.519 and 10.548 MHz for β-$WCl_6$, in excellent agreement with previous results (**Figures 2 (D-E)**). The quadrupolar parameters extracted for β-$WCl_6$ from NQR experiments are so similar, that not even experiments at 21.1 T could effectively separate these patterns; hence, no further NMR experimentation was carried out.

It is clear that NMR and NQR are ideal partners for studying polymorphs, especially in cases where there is no *a priori* knowledge of the quadrupolar parameters. The specificity of the NQR experiment, while valuable for differentiating sites with similar quadrupolar parameters, is also a crutch, in that it results in tedious searches for NQR resonances over broad frequency ranges. However, the UW SSNMR experiments are capable of providing rapid and accurate determinations of quadrupolar parameters, allowing for the NQR experiment to be conducted in a frequency region of high specificity, and forgoing the monotonous, long "search periods" associated with conventional NQR experimentation.

In both α-$WCl_6$ and β-$WCl_6$, the $C_Q$ values are at the lower end of the range of values reported for a chlorine directly bound to a transition metal.[74] As well, the values of $\eta_Q$ are close to zero, indicating that the $^{35}Cl$ EFG tensors are nearly axially symmetric in each case, and that the chlorine atoms are in environments of high cylindrical symmetry. This is expected for chlorine atoms that are in terminal bonding arrangements

with respect to the central metal atom, and indicates that $V_{33}$ is likely to be oriented directly along or close to the direction of the metal-chlorine bond (*vide infra*).

Plane-wave DFT calculations of the $^{35}$Cl EFG tensors for both the α- and β-forms of $WCl_6$ are presented in **Table 2**. In both forms of the compound, the values of $C_Q$ are found to be negative (consistent with the terminal chlorine site) and consistently lower in magnitude than the experimental values. The values of $\eta_Q$ are predicted to be near zero, also in agreement with experiment. The calculated $^{35}$Cl NMR parameters obtained prior to optimization of the structure are in poorer agreement with experiment, highlighting the need for geometry optimization of the structures. For example, in the set of calculations on model systems of β-$WCl_6$ without geometry optimization, there is a large range of $C_Q$ values predicted, which is not expected for chlorine environments that are chemically very similar. This suggests that the reported crystal structure of β-$WCl_6$ may be inaccurate, as geometry optimization of the structure yields quadrupolar parameters that are more consistent with the $^{35}$Cl SSNMR data, and not subject to wild variations from site to site. It is also important to note that the predicted quadrupolar parameters are not ideal (i.e., quite far from experimental values) for use as *a priori* starting points for the acquisition of NQR spectra; however, NQR experiments featuring the use of WURST pulses may be useful in this respect.[75]

The theoretically determined $^{35}$Cl EFG tensor orientations for α- and β-$WCl_6$ are shown in **Figures 3(A)** and **3(B)**, respectively. In both cases, the largest principal components of each $^{35}$Cl EFG tensor, $V_{33}$, are oriented along, or nearly along the W–Cl bonds ($\angle V_{33}$-Cl-W = 178° for α-$WCl_6$ and 180° for β-$WCl_6$). The value of $\eta_Q$ is close to

zero in both forms, so the orientations of $V_{11}$ and $V_{22}$ are of little consequence, since $V_{11} \approx V_{22}$.

*Tetracholorotungsten(VI) oxide ($WOCl_4$) and tetrachloromolybdenum(VI) oxide ($MoOCl_4$)*

The crystal structure of $WOCl_4$ has one molecule in the asymmetric unit with four chlorine atoms in magnetically equivalent environments ($r$(W-Cl) = 2.285 Å).[76] The molecule has a square pyramidal structure with an oxygen atom double bonded to the central tungsten atom at the apex (**Scheme 1**). The chlorine atoms sit in a square plane, which lies slightly below the plane of the tungsten atoms. Previous XRD studies of $WOCl_4$ have suggested that the molecules are associated through weak interactions between the oxygen of one molecule and the tungsten of another. The molecules stack on top of one another to form linear arrays with asymmetric W–O–W bridges (the intramolecular W–O distance is 1.737 Å, whereas the intermolecular W–O distance is 2.258 Å).

The local molecular structure of $MoOCl_4$ is similar to that of $WOCl_4$ (**Scheme 1**); however, their extended structures are strikingly different. Neutron and X-ray diffraction studies have shown that $MoOCl_4$ contains two molecules in the asymmetric unit with four chemically and magnetically distinct chlorine sites. The square pyramidal units do not form linear arrays, but instead, are associated through weak interactions between the chlorine atoms of one molecule and the molybdenum atom of another (the Mo–Cl bond length is *ca.* 2.3 Å, and the intermolecular Mo···Cl distance is 2.9 Å). These intermolecular interactions cause the molecules to form *quasi*-dimeric structures, with a

single chlorine from each molecule forming the *pseudo*-bridge between adjacent pyramidal units.[77]

The $^{35}$Cl SSNMR spectra for $WOCl_4$ and $MoOCl_4$ are shown in **Figures 4(A)** and **(B)**, respectively. The CT of the $WOCl_4$ pattern has a breadth of ca. 1075 kHz. The appearance of the discontinuities indicates that there is only one chlorine environment within the complex, in agreement with the aforementioned structure. The markedly different appearance of the $^{35}$Cl SSNMR spectrum for $MoOCl_4$ clearly reflects the structural differences between the two complexes. The discontinuities in the $MoOCl_4$ spectrum are less well defined than those in the $WOCl_4$ spectrum, and it appears that there are at least four discernible patterns, three of which are very similar and overlapping with each other. The spectrum for $MoOCl_4$ has a much larger breadth (*ca*. 1750 kHz) than that of $WOCl_4$ and exhibits notable distortions, with greater intensity apparent in the high-frequency region of the spectrum.

The $WOCl_4$ spectrum is best simulated with a single site $C_Q$ = 26.05 MHz and $\eta_Q$ = 0.115 (**Table 1**). The $MoOCl_4$ spectrum is simulated with four overlapping patterns of equal intensity arising from chlorine environments with distinct quadrupolar parameters (**Table 1**). Three of the patterns have values of $C_Q$ and $\eta_Q$ that lie within experimental error of one other, indicating that there are three chlorine sites with similar chemical environments. The resulting overlap of these three patterns causes broadening of the outer discontinuities.

The magnitudes of $C_Q$ for $WOCl_4$ and $MoOCl_4$ are considerably larger than that of $WCl_6$ (**Table 1**); it is not trivial to explain this difference, given the distinct modes of bonding in and different symmetries of these two sets of compounds. In particular, one

must be cautious in looking for relationships between M-Cl bond lengths and magnitudes of $C_Q$. The natures of the M-Cl bonds in $WCl_6$ are likely to be very different from those in the $MOCl_4$ species, despite the very similar M-Cl bond lengths (i.e., by natures, we mean the differences in bonds in terms of their covalent/ionic character, hybridization of *s* and *p* orbitals, and multiple bond character).[78] Even the comparison of the structurally similar $WOCl_4$ and $MoOCl_4$ species does not reveal any simple explanation for the variation in values of $C_Q$ (clearly the nature of the extended structure in the latter case plays a role in influencing the EFG tensor). The value of $\eta_Q$ for $WOCl_4$ is comparable to that of $WCl_6$ and is consistent with previous observations for terminal chlorine environments. The values of $\eta_Q$ for $MoOCl_4$ are all moderate, indicating non-axial EFG tensors, and reflecting the association of the molecules into dimeric structures. Indeed, a careful analysis of the contributions from individual molecular orbitals to the EFG tensor is necessary to account for differences in values of $C_Q$, as well as for examining the relationships between intra- and intermolecular contacts and EFG tensor orientations and parameters (*vide infra*).[65]

Both $WOCl_4$ and $MoOCl_4$ systems have previously been studied by $^{35}Cl$ NQR spectroscopy and similar results regarding the types and multiplicities of chlorine environments were found. The NQR spectrum for the $WOCl_4$ complex has a single peak corresponding to the single chlorine chemical environment, and the value of the NQR frequency is in good agreement with the experimentally determined value of $C_Q$ (**Table 2**). The spectrum of the $MoOCl_4$ complex has four NQR frequencies, three of which are very similar. The highest frequency resonance (ca. 3 MHz higher than the others) was

assigned to the chlorine atoms which act as the *pseudo*-bridge between the metal centres.[72] This is consistent with our findings discussed above.

Plane-wave DFT calculations were performed for $WOCl_4$ and $MoOCl_4$ using structures obtained from the ICSD. The DFT calculations of the $^{35}Cl$ EFG tensors for $WOCl_4$ predict one magnetically distinct chlorine environment, as expected. The value of $C_Q$ predicted from post-geometry optimized calculations is found to be negative, and $\eta_Q$ close to zero, consistent with the chlorine atoms being in a terminal environment. The theoretical magnitudes of $C_Q$ are considerably lower than the experimentally determined values, but the values of $\eta_Q$ are more closely reproduced. $^{35}Cl$ DFT calculations completed for $MoOCl_4$ predict four chlorine environments, all with negative values of $C_Q$ and moderate values of $\eta_Q$, consistent with our assignments above.

The $^{35}Cl$ EFG tensor orientations for $WOCl_4$ and $MoOCl_4$ are shown in **Figures 3(C)** and **(D)** respectively. Since the value of $\eta_Q$ is near zero for the single chlorine site in $WOCl_4$, this indicates that $V_{33}$ is the distinct component in the $^{35}Cl$ EFG tensor and that the values of $V_{11}$ and $V_{22}$ are similar in magnitude. Due to the symmetry of the $WOCl_4$ molecule, the presence of the chlorine atoms in a plane below the tungsten atom, and the covalently bound O atom, $V_{33}$ is not oriented exactly along the W–Cl bond (i.e., $\angle(V_{33}$-Cl-W = 4.45°). In $MoOCl_4$, the three magnetically distinct chlorine sites (the pseudo-bridging chlorine atom (Cl1), the terminal chlorine atom opposite to the pseudo-bridge (Cl2), and the terminal chlorine atom adjacent to the pseudo-bridge (Cl3 and Cl4)) have distinct $^{35}Cl$ EFG tensor orientations. The designation *pseudo-bridging* refers to a chlorine atom that has a covalent bond with one metal centre, and a distant contact with a second metal centre from a neighbouring molecule. All three sites have moderate values

of $\eta_Q$, indicating that their $^{35}$Cl EFG tensors are not axially symmetric, which is indicative of an absence of cylindrical symmetry of the ground-state electron density about these chlorine sites. For Cl1, $V_{33}$ is oriented near the Mo–Cl bond ( $\angle$($V_{33}$-Cl-Mo = 1.85°) and the value of $C_Q$ is negative, which is consistent with similar observations for terminal chlorine environments.[45] It has been shown that chlorine atoms which are involved in true bridging interactions between transition metal centres have $^{35}$Cl EFG tensor orientations in which $V_{33}$ is oriented perpendicular (or approximately perpendicular) to the plane of the M–Cl–M bonding arrangement and positive values of $C_Q$.[46] Sites Cl2, Cl3 and Cl4 all have the $V_{33}$ components directed near the direction of their respective Mo–Cl bonds ($\angle$($V_{33}$-Cl-Mo = 5.67° and 12.95°, respectively), as is typical of chlorines in terminal bonding arrangements.

*Niobium(V) chloride ($NbCl_5$) and tantalum(V) chloride ($TaCl_5$)*

The crystal structure of niobium pentachloride ($NbCl_5$) has one molecule in the asymmetric unit with nine crystallographically distinct chlorine atoms. The complex forms a dimeric structure in which the chlorine atoms form two octahedra sharing a common edge, with the niobium atoms occupying the centres of the octahedra. This structure results in three specific bonding arrangements for the chlorine atoms: bridging ($Cl_{br}$), terminal-axial ($Cl_{ax}$) and terminal-equatorial ($Cl_{eq}$) (**Scheme 1(D)**). The average Nb–Cl bond distances are 2.555, 2.302 and 2.250 Å for $Cl_{br}$, $Cl_{ax}$ and $Cl_{eq}$, respectively.[79] Tantalum(V) chloride ($TaCl_5$) is isostructural to $NbCl_5$, and has average Ta–Cl bond lengths of 2.547, 2.307 and 2.225 Å for $Cl_{br}$, $Cl_{ax}$ and $Cl_{eq}$, respectively.[80]

The static $^{35}$Cl SSNMR spectra of $NbCl_5$ and $TaCl_5$ are shown in **Figures 5(A)** and **(B),** respectively. The CT patterns have breadths of *ca*. 1300 kHz ($NbCl_5$) and *ca*. 1400 kHz ($TaCl_5$). For each system, the outer manifolds of the spikelet patterns reveal several clearly defined discontinuities that indicate the presence of three distinct patterns, consistent with the presence of the $Cl_{br}$, $Cl_{ax}$ and $Cl_{eq}$ bonding environments (*vide infra*).

The analytical simulation for the entire powder pattern of $NbCl_5$ is shown in **Figure 5(A)** as the red trace, with the individual patterns shown as the blue ($C_Q$ = 25.30 MHz and $\eta_Q$ = 0.385), green ($C_Q$ = 15.0 MHz and $\eta_Q$ = 0.081) and orange ($C_Q$ = 14.70 MHz and $\eta_Q$ = 0.655) traces. We note that the patterns are simulated with 1:1:1 signal intensity (instead of the expected 1:2:2, $Cl_{br}$:$Cl_{ax}$:$Cl_{eq}$) as the WURST-CPMG technique is non-quantitative (since each Cl site is likely to have a slightly different $T_2$ constant) and the relative signal intensity does not accurately reflect the relative populations of the individual chlorine environments. Using results obtained via DFT calculations (*vide infra*), it is possible to assign the three patterns in the spectrum to the specific chlorine bonding environments. The pattern with the largest absolute magnitude of $C_Q$ corresponds to the $Cl_{br}$ environment, consistent with the results obtained for $Cp^*ZrCl_3$ in the study by Rossini *et al*.,[46] but distinct from those for bridging chlorine sites in main group compounds.[45] This suggests that the value of $C_Q$ for the bridging chlorine is strongly dependent on the nature of the metal to which it is bonded, as well as the overall structure of the complex. The $Cl_{br}$ has a moderate value of $\eta_Q$, as is typical for this type of environment. The pattern with the value of $\eta_Q$ close to zero is assigned to the $Cl_{ax}$, again consistent with high cylindrical symmetry about such terminal M–Cl bonds. The final pattern has a value of $\eta_Q$ closest to unity and is assigned to the $Cl_{eq}$, which differs

from results obtained by Rossini *et al*. where it was found that terminal chlorine environments had values of $\eta_Q$ close to zero. Since the values of $C_Q$ for the two types of terminal sites are almost identical, it is clear that $\eta_Q$ is useful for their differentiation.

In a similar manner, analytical simulations of the entire $^{35}$Cl CT pattern, as well as the three contributing patterns, are shown in **Figure 5(B)** for $TaCl_5$. The site assignments are identical to those described for $NbCl_5$. The values for $C_Q$ for all three sites of $TaCl_5$ are larger than the corresponding values for $NbCl_5$. Since $NbCl_5$ and $TaCl_5$ are isostructural, and tantalum is one row below niobium in the periodic table, it is the relative size of the metal atom which appears to influence the magnitude of the quadrupolar interaction, with the larger central metal atom corresponding to a larger value of $C_Q$. Interestingly, the M–Cl bond lengths are very similar in these two systems, with the largest difference being 0.03 Å, again discouraging the invoking of simple correlations between bond length and $C_Q$.

Both of these complexes were previously studied by $^{35}$Cl NQR spectroscopy, with the measured quadrupolar frequencies given in **Table 2**. The room temperature NQR study of $NbCl_5$ reveals seven distinct sites, five of which have comparable NQR frequencies. The two remaining sites have substantially higher NQR frequencies, and are assigned to $Cl_{br}$, which is consistent with our results.[72] Similar NQR results were found for $TaCl_5$,[81] and are also consistent with this work.

Plane-wave DFT calculations of $^{35}$Cl EFG tensors were performed on $NbCl_5$ and $TaCl_5$ (**Table 2**). Calculated values of $C_Q$ and $\eta_Q$ distinguish bridging and terminal chlorine sites, not only by the absolute magnitudes of $C_Q$, but also by their signs: bridging and terminal chlorines have positive and negative values of $C_Q$, respectively. The

CASTEP calculations for post-geometry optimized $NbCl_5$ and $TaCl_5$ models are in good agreement with experimental values of $C_Q$ and reasonable agreement for values of $\eta_Q$ (**Figure 1**).

The theoretical $^{35}Cl$ EFG tensor orientations were determined for both complexes. Since they are isostructural, only the results for $NbCl_5$ are shown in **Figure 3(E)**. The $Cl_{br}$ sites, which have moderate values of $\eta_Q$, have $V_{33}$ components oriented nearly perpendicular (90.30°) to the M–Cl–M plane, which is consistent with observations by Rossini *et al.*[46] The moderate values of $\eta_Q$ for these sites indicate that the $^{35}Cl$ EFG tensor is non-axial (i.e., $V_{11} \neq V_{22}$), which is consistent with the local geometry of a $Cl_{br}$ atom. The $Cl_{ax}$ sites have values of $\eta_Q$ close to zero, with $V_{33}$ components oriented near the directions of the M–Cl bonds in each case, as expected. Finally, the $Cl_{eq}$ sites have large values of $\eta_Q$, indicating that $V_{11}$ is the distinct component of the $^{35}Cl$ EFG tensor (i.e., the absolute magnitudes of $V_{22}$ and $V_{33}$ are similar). In each system, $V_{11}$ is oriented towards the bridging chlorine environments, and $V_{33}$ is directed near the M–Cl bonds, in good agreement with previous studies.

*$^{35}Cl$ Transverse Relaxation Time ($T_2$) measurements*

As mentioned above, the $^{35}Cl$ SSNMR spectra obtained for each of the compounds investigated exhibit variations in spectral intensity that do not precisely match the intensities produced from analytical simulations. For example, higher intensity is consistently observed in the high-frequency (leftmost) regions of the spectra. While there are no detailed studies in literature that investigate this phenomenon, we have reported instances of this intensity variation in several other papers on ultra-wideline

NMR of quadrupolar nuclei.[47,82] We speculate that it may be caused by two factors: (*i*) tuning limitations of the probe used that may cause uneven excitation/detection across the range of frequencies studied and/or (*ii*) variation of the transverse relaxation times across the breadth of the pattern, which we refer to as $T_2$ *anisotropy*.

In order to investigate this further, we measured the transverse relaxation time constants across the patterns by placing the transmitter at frequencies corresponding to different discontinuities of the patterns, and acquiring a series of echoes using a CPMG experiment. By plotting the echo intensity against the echo time and fitting the data to an exponential decay, the $T_2$ values and their associated errors were determined. The process is shown for $WCl_6$ in **Figure 6** and the remaining data is shown in the Supporting Information (**Table S8**). We found that in most cases, $T_2$ values measured at the low-frequency discontinuities are smaller than those measured at higher frequency. The overall differences in $T_2$ values are not large, certainly well under an order of magnitude. At this time, it is unclear that the tuning characteristics of the probe are responsible for any of the intensity variation, since we have used the exact same probes and tuning configurations to acquire spectra where the intensity variations do not follow the patterns described above. Clearly, a more detailed study of this intensity variation is required; if $T_2$ anisotropy is solely responsible for this phenomenon, some interesting physical models and chemical interpretations could arise in the future.

*LMO Analysis of the $^{35}$Cl EFG Tensors*

Upon examining the results obtained for the dimer pentahalide species, certain questions arise: (*i*) why do the $Cl_{br}$ sites have significantly larger values of $C_Q$ compared

to the terminal chlorines, and (*ii*) why do the $Cl_{eq}$ sites have values of $\eta_Q \approx 1$ when the $Cl_{ax}$ have values of $\eta_Q \approx 0$? In order to further probe the origins of the $^{35}Cl$ EFG tensors for the various chlorine environments in the pentahalide species, we performed Localized Molecular Orbital (LMO) analysis, in which the contributions of each LMO to the $^{35}Cl$ EFG tensors are determined.[65] The LMOs are quantum-mechanical representations of bonds and lone pairs as well as core shell electron pairs. For $Nb_2Cl_{10}$, there are also three-centre μ-bonding LMOs centred on the bridging chlorine atoms. Here, we chose to conduct calculations and analysis upon the $Nb_2Cl_{10}$ dimer, which possesses distinct types of terminal and bridging chlorine sites. We note that DFT MO calculations and concomitant LMO analyses were only conducted upon $Nb_2Cl_{10}$ clusters, since these species are sufficiently isolated from surrounding lattice that $^{35}Cl$ EFG tensors are not adversely affected by long-range electrostatic interactions. Compounds like α-$WCl_6$, β-$WCl_6$ and $MoOCl_4$ all feature shorter intermolecular contacts that may influence the $^{35}Cl$ EFG tensors, so LMO analyses on isolated clusters from these systems were not conducted (a full study of inter- and intramolecular electrostatic effects on EFG tensors for all of these systems is beyond the scope of the current work).

The $^{35}Cl$ EFG tensor parameters calculated using ADF and CASTEP are in good agreement with one another as well as the experimentally obtained parameters (**Table S10**). This indicates that the $^{35}Cl$ EFG tensor parameters are highly dependent upon EFGs originating within the individual $Nb_2Cl_{10}$ units, and almost independent of EFGs arising from intermolecular interactions within the solid. Furthermore, geometry optimization of the structure improves the agreement between the calculated parameters and those obtained experimentally.

The contribution of each LMO to the principal components of the $^{35}$Cl EFG tensors are tabulated in **Table 3**, and the atom labels for the $Nb_2Cl_{10}$ unit are shown in **Figure 7(A)**. The individual LMOs that contribute to the EFGs are shown in **Figure 7(B)** as isosurfaces.[65] The calculations describe contributions from core, lone-pair (LP, with the π and σ referring to local symmetry with respect to the metal-chlorine bond axis), dative Nb-Cl σ-bonds, π-bonds and 3-centred bridging μ-bonds. Graphical representations of the $^{35}$Cl EFG tensors for the distinct chlorine environments ($Cl_{ax}$, $Cl_{aeq}$ and $Cl_{br}$) in the form of polar plots (EFG in the direction of the electric field) are shown in **Figure 8**. The blue regions of the graphical representations correspond to positive EFGs and the orange regions represent negative EFGs.

The case of the $Cl_{ax}$ environment is the most straightforward and agrees with previous findings in the literature for terminal chlorines.[46] The largest component of the EFG tensor, $V_{33}$, is positive and oriented roughly parallel to the Nb-Cl bond axis (**Figure 8(A)**), indicating a loss of electron density in this direction to the covalent Cl-Nb interactions. The σ($Cl_{ax}$-Nb) (**MO1)** and the σ LP $Cl_{ax}$ (**MO2)** LMOs both make large negative contributions to the value of $V_{33}$ (**Table 3**). The π LPs (**MO3** and **MO4**) make large positive contributions that outweigh those of the σ orbitals and therefore, the overall $V_{33}$ for the $Cl_{ax}$ is positive. The axial symmetry of the EFG tensor at the $Cl_{ax}$, with a value of $\eta_Q$ close to 0, is due to the cylindrical electronic distribution about the nucleus caused by contributions of **MO3** and **MO4** to $V_{11}$ and $V_{22}$ that are roughly equal in magnitude but opposite in sign.

Like the $Cl_{ax}$, the $Cl_{eq}$ sites also have a positive $V_{33}$, which is oriented along the direction of the Nb-Cl bond (**Figure 8(B)**). The σ($Cl_{eq}$-Nb) (**MO5**) and σ LP $Cl_{eq}$ (**MO6**)

orbitals cause large negative contributions to $V_{33}$, in a similar manner to the terminal-axial chlorine atoms. The $\pi(Cl_{eq}\text{-Nb})$ (**MO7**) and the $\pi_z$ LP $Cl_{eq}$ (**MO8**) orbitals make positive contributions to $V_{33}$ that outweigh those of the $\sigma$ orbitals, and results in an overall positive EFG. The $\pi$ orbitals of the $Cl_{eq}$ contribute quite differently to the values of $V_{11}$ and $V_{22}$. **MO7** generates a negative contribution to $V_{11}$ and a positive contribution to $V_{22}$, whereas **MO8** makes a positive contribution to $V_{11}$ and an even larger negative contribution to $V_{22}$. The unequal contribution to $V_{11}$ and $V_{22}$ of **MO7** and **MO8** is reflected in the large asymmetry parameter of the $^{35}$Cl EFG tensor ($\eta_Q$ is near unity). This is contrasted to the case of the $Cl_{ax}$, in which equal involvement from the orbitals with $\pi$ symmetry leads to an axially symmetric tensor with $\eta_Q$ close to zero.

For the $Cl_{br}$, $V_{33}$ is oriented perpendicular to the equatorial plane formed by the two Nb atoms and the $Cl_{br}$ atom (**Figure 8(C)**), as is typical for bridging chlorines.[47] The $Cl_{br}$ environment consists of two equivalent, weakly covalent Nb-$Cl_{br}$ orbitals per Cl atom at an angle of 102° and two relatively "pure" LP orbitals. The orbitals in the plane of the Nb-Cl-Nb bond ($\pi_x$ LP $Cl_{br}$ (**MO9**) , $\mu$(Nb-Cl-Nb) (**MO10**) and $\sigma$ LP $Cl_{br}$ (**MO11**)) create positive contributions to $V_{33}$; however, these contributions are outweighed by the enormous negative contribution made by the out-of-plane $\pi_z$ LP $Cl_{br}$ (**MO12**). **MO12** is almost entirely non-covalent in nature and therefore, contributes very strongly to the EFG. The result is a large, negative $V_{33}$ at the $Cl_{br}$ nuclei which is oriented in the direction of the lone-pair (**MO12**). The moderate value of $\eta_Q$ for the $Cl_{br}$ nuclei is caused by unequal contributions of the in-plane orbitals (**MO9**, **MO10** and **MO11**) to $V_{11}$ and $V_{22}$.

*$^{35}$Cl SSNMR of $WCl_6$ supported on silica*

$WCl_6$ has been grafted onto a silica support material, as described in the Experimental Section. Our aim in the current work was to see if it was possible to acquired a high quality spectrum of this sample in a reasonable time frame, and make comparisons between this new spectrum and some of the spectra of the tungsten chlorides discussed herein. Only two other attempts at acquiring $^{35}$Cl SSNMR spectra of such systems have been reported, by our group (silica-supported $TiCl_4$),[47] and by Mania *et al*. (silica-supported $TiCl_4$).[26] The $^{35}$Cl SSNMR spectrum of this sample, acquired using the WURST-CPMG pulse sequence at a field of 18.8 T is shown in **Figure 9**. The spectrum was acquired in a single experiment (i.e., no piecewise acquisitions), over a period of ca. 15.8 hours. It is noted that the long experimental times are a result of the low weight percentage of $WCl_6$ loaded onto the silica support material (W wt% = 5.48%). The CT powder pattern spans a range of just over 1.2 MHz, which is far wider than that observed for the spectrum of pure $\alpha$-$WCl_6$, which spans only ca. 650 kHz at 21.1 T (it would span ca. 740 kHz at 18.8 T, **Figure S20**). Simulations of the spectrum of grafted $WCl_6$ yield $C_Q$ = 25.98(5) MHz and $\eta_Q$ = 0.11(1), which are far different values from those of pure $WCl_6$ ($C_Q$ = 21.0(1) MHz and $\eta_Q$ = 0.029(5)). In fact, this new set of quadrupolar parameters bare a striking resemblance to those of $WOCl_4$ ($C_Q$ = 26.05(10), $\eta_Q$ = 0.115(5)), which suggests that a major change in the structure and bonding of $WCl_6$ has taken place. A full structural analysis and interpretation of this result is currently underway, and beyond the scope of the current work; however, we have again demonstrated that it is possible to acquire high quality ultra-wideline $^{35}$Cl SSNMR

spectra of diluted, surface-bound species, and that such spectra are potentially very rich in structural information.

**Conclusions**

Using the WURST-CPMG pulse sequence and the VOCS technique we have demonstrated it is possible to acquire broad $^{35}$Cl SSNMR powder patterns for diamagnetic chlorine-containing TM complexes exhibiting a variety of structural motifs. The experiments were conducted at both moderate (9.4 T) and ultra-high (21.1 T) magnetic field strengths, with the latter affording great reductions in experimental times due to increases in S/N ratios and reductions in CT pattern breadths. The $^{35}$Cl SSNMR spectra prove to be very useful as probes of structure, due to the sensitivity of the $^{35}$Cl EFG tensors to both subtle and significant differences in molecular geometry and chemical environment.

The $^{35}$Cl SSNMR spectra of $\alpha$-$WCl_6$ and $\beta$-$WCl_6$ were acquired but were not of high enough resolution to differentiate the two polymorphic forms; however, they could be differentiated by $^{35}$Cl NQR experiments. This highlights the efficacy of using SSNMR and NQR in tandem; the rapid acquisition of the SSNMR spectra provides an estimation of the quadrupolar parameters and substantially refines the frequency region in which to search for NQR signal. The effects of molecular packing in the solid state were also visible in the $^{35}$Cl SSNMR spectra of $WOCl_4$ and $MoOCl_4$. The $WOCl_4$ molecules stack in symmetric linear arrays resulting in a single chlorine environment whereas the $MoOCl_4$ complex forms *quasi*-dimeric structures resulting in several distinct chlorine environments (i.e., pseudo-bridging and terminal). In the dimeric pentahalide complexes,

$NbCl_5$ and $TaCl_5$, the individual chlorine environments were distinguished based on their values of $C_Q$. It was found that the $Cl_{br}$ environments had larger values of $C_Q$ when compared to the terminal chlorine environments. Furthermore, the two terminal chlorine environments, $Cl_{ax}$ and $Cl_{eq}$, could be distinguished based on their values of $\eta_Q$, the former having values close to 0 and the latter having values close to unity. It was also observed that the tantalum complex had larger values of $C_Q$ for all chlorine environments, suggesting that the size of the metal centre influences the value of $C_Q$.

Plane-wave DFT calculations were completed for each complex. The $^{35}Cl$ EFG tensor parameters were found to be in generally good agreement with experimental results especially in systems in which intermolecular interactions have little influence on the $^{35}Cl$ EFG. The theoretical $^{35}Cl$ EFG tensor orientations reveal that $V_{33}$ is directed either along or near the M-Cl bond for chlorine atoms in terminal bonding environments. Conversely, for chlorine atoms in bridging bonding environments, $V_{33}$'s are oriented approximately perpendicular to the M-Cl-M planes. An LMO analysis completed on the $NbCl_5$ system revealed that the $^{35}Cl$ NMR parameters are determined by the composition and relative orientations of the MOs participating in bonding to chlorine. The $\eta_Q$ value close to zero for the $Cl_{ax}$ arises from equivalent contributions of the $\pi$ LP orbitals to $V_{11}$ and $V_{22}$ whereas the $\pi$ orbitals for the $Cl_{eq}$ do not contribute equivalently, leading to an $\eta_Q$ close to unity. The large value of $C_Q$ for the $Cl_{br}$ arises from the large, negative contribution of the $\pi_z$ LP orbital that is perpendicular to the Cl-M-Cl plane, because positive contributions from other orbitals centred on $Cl_{br}$ are reduced due to the true Cl-Nb covalency.

We also demonstrated the application of $^{35}$Cl SSNMR to the study of a transition-metal catalyst that has been grafted onto a silica support material. The resulting spectrum is drastically different than the bulk species, indicating that the structure of the $WCl_6$ species changes upon grafting. Given the rapidity with which the $^{35}$Cl SSNMR spectra can be acquired, and the fact that "focused" NQR experiments can be conducted in the wake of SSNMR experiments to examine site specificities, we believe that an enormous number of chlorinated transition-metal complexes can be structurally probed in both the bulk and supported forms. We hope to establish this protocol as a strong basis for the study of chlorine-containing transition-metal complexes, and extend this study to catalytic systems of increasing complexity, with the aim of studying immobilized heterogeneous catalysts with very dilute chlorine contents.

**Acknowledgments**

R.W.S. thanks NSERC for funding this research in the form of a Discovery Grant and Discovery Accelerator Supplement. R.W.S. is also grateful for an Early Researcher Award from the Ontario Ministry of Research and Innovation. We are also grateful for the funding of the Laboratories for Solid-State Characterization at the University of Windsor from the Canadian Foundation for Innovation, the Ontario Innovation Trust, and the University of Windsor. This work was made possible, in part, by the facilities of the Shared Hierarchical Academic Research Computing Network (SHARCNET: http://www.sharcnet.ca). We are grateful to Dr. Victor Terskikh at the National Ultrahigh-field NMR Facility for Solids in Ottawa, Ontario, Canada (http://nmr900.ca/), as well as Dr. Kristopher Harris, for acquiring $^{35}$Cl SSNMR data at 21.1 T.

**Supporting Information Available**: Details on NMR acquisition parameters, pXRD patterns, additional $^{35}$Cl SSNMR data, details on computational chemistry and LMO analysis, and analytical simulations of $^{35}$Cl SSNMR spectra.

## References


(1) Ajiboye, S. I.; Iqbal, J.; Peacock, R. D.; Prouff, N.; Taylor, G. J.; Winfield, J. M.; Liu, X. *Fluor. Chem.* **1998**, *91*, 213–218.

(2) Englert, U.; Pampaloni, G.; Puccini, F.; Volpe, M. *J. Organomet. Chem.* **2007**, *692*, 3144–3150.

(3) Sim, A.; Cant, N. W.; Trimm, D. L. *Int. J. Hydrog. Energy* **2010**, *35*, 8953–8961.

(4) Nguyen, A. I.; Blackmore, K. J.; Carter, S. M.; Zarkesh, R. A.; Heyduk, A. F. *J. Am. Chem. Soc.* **2009**, *131*, 3307–3316.

(5) Mokdsi, G.; Harding, M. M. *J. Inorg. Biochem.* **2001**, *86*, 611–616.

(6) Waern, J. B.; Harris, H. H.; Lai, B.; Cai, Z.; Harding, M. M.; Dillon, C. T. *J. Biol. Inorg. Chem.* **2005**, *10*, 443–452.

(7) Köpf-Maier, P.; Klapötke, T. *J. Cancer Res. Clin. Oncol.* **1992**, *118*, 216–221.

(8) Matthias, B. T.; Geballe, T. H.; Geller, S.; Corenzwit, E. *Phys. Rev.* **1954**, *95*, 1435.

(9) Raub, C. J.; Sweedler, R.; Jensen, M. A.; Broadston, S.; Matthiasg, T. *Phys. Rev. Lett.* **1964**, *13*, 746–747.

(10) Bukowski, Z.; Badurski, D.; Stepien-Damm, J.; Troc, R. *Solid State Commun.* **2002**, *123*, 283–286.

(11) Nowak, I.; Ziolek, M. *Chem. Rev.* **1999**, *99*, 3603–3624.

(12) Tanabe, K.; Okazaki, S. *Appl. Catal. A* **1995**, *133*, 191–218.

(13) Wallace, K. C.; Liu, A. H.; Davis, W. M.; Schrock, R. R. *Organomet.* **1989**, *8*, 644–654.

(14) Ushikubo, T.; Wada, K. *J. Catal.* **1994**, *148*, 138–148.

(15) Schrock, R. R.; Hoveyda, A. H. *Angew. Chem. Int. Ed.* **2003**, *42*, 4592–4633.

(16) Yandulov, D. V; Schrock, R. R. *Science (80-. ).* **2003**, *301*, 76–78.

(17) Balcar, H.; Čejka, J.; Sedláček, J.; Svoboda, J.; Zedník, J.; Bastl, Z.; Bosáček, V.; Vohlídal, J. *J. Mol. Catal. A* **2003**, *203*, 287–298.

(18) Garrett, C. E.; Prasad, K. *Adv. Synth. Catal.* **2004**, *346*, 889–900.

(19) Collman, J. P.; Hegedu, L. S.; Cooke, M. P.; Norton, J. R.; Dolcetti, G.; Marquardt, D. N. *J. Am. Chem. Soc.* **1972**, *94*, 1789–1790.

(20) Dumont, W.; Poulin, J.; Dang, T.; Kagan, H. B. *J. Am. Chem. Soc.* **1973**, *95*, 8295–8299.

(21) Maschmeyer, T.; Rey, F.; Sankar, G.; Thomas, J. M. *Nature* **1995**, *378*, 159–162.

(22) Eisen, M. S.; Marks, T. J. *J. Am. Chem. Soc.* **1992**, *114*, 10358–10368.

(23) Joubert, J.; Delbecq, F.; Sautet, P.; Le Roux, E.; Taoufik, M.; Thieuleux, C.; Blanc, F.; Copéret, C.; Thivolle-Cazat, J.; Basset, J.-M. *J. Am. Chem. Soc.* **2006**, *128*, 9157–9169.

(24) Blanc, F.; Thivolle-Cazat, J.; Basset, J.-M.; Copéret, C.; Hock, A. S.; Tonzetich, Z. J.; Sinha, A.; Schrock, R. R. *J. Am. Chem. Soc.* **2007**, *129*, 1044–1045.

(25) Blanc, F.; Basset, J.-M.; Copéret, C.; Sinha, A.; Tonzetich, Z. J.; Schrock, R. R.; Solans-Monfort, X.; Clot, E.; Eisenstein, O.; Lesage, A.; Emsley, L. *J. Am. Chem. Soc.* **2008**, *130*, 5886–5900.

(26) Mania, P.; Verel, R.; Jenny, F.; Hammond, C.; Hermans, I. *Chem. Eur. J.* **2013**, *19*, 9849–9858.

(27) Blanc, F.; Copéret, C.; Lesage, A.; Emsley, L. *Chem. Soc. Rev.* **2008**, *37*, 518–526.

(28) Zhang, W.; Xu, S.; Han, X.; Bao, X. *Chem. Soc. Rev.* **2012**, *41*, 192–210.

(29) Jezequel, M.; Dufaud, V.; Ruiz-Garcia, M. J.; Carrillo-Hermosilla, F.; Neugebauer, U.; Niccolai, G. P.; Lefebvre, F.; Bayard, F.; Corker, J.; Fiddy, S.; Evans, J.; Broyer, J. P.; Malinge, J.; Basset, J. M. *J. Am. Chem. Soc.* **2001**, *123*, 3520–3540.

(30) Ahn, H.; Marks, T. J. *J. Am. Chem. Soc.* **2002**, *124*, 7103–7110.

(31) Le Roux, E.; Chabanas, M.; Baudouin, A.; de Mallmann, A.; Coperet, C.; Quadrelli, E. A.; Thivolle-Cazat, J.; Basset, J.; Lukens, W.; Lesage, A.; Emsley, L. *J. Am. Chem. Soc.* **2004**, *126*, 13391–13399.

(32) Hung, I.; Schurko, R. W. *J. Phys. Chem. B* **2004**, *108*, 9060–9069.

(33) Lo, A. Y. H.; Bitterwolf, T. E.; Macdonald, C. L. B.; Schurko, R. W. *J. Phys. Chem. A* **2005**, *109*, 7073–7087.

(34) Hamaed, H.; Lo, A. Y. H.; Lee, D. S.; Evans, W. J.; Schurko, R. W. *J. Am. Chem. Soc.* **2006**, *128*, 12638–12639.

(35) Rossini, A. J.; Hung, I.; Schurko, R. W. *J. Phys. Chem. Lett.* **2010**, *1*, 2989–2998.

(36) Rossini, A. J.; Hung, I.; Johnson, S. A.; Slebodnick, C.; Mensch, M.; Deck, P. A.; Schurko, R. W. *J. Am. Chem. Soc.* **2010**, *132*, 18301–18317.

(37) Larsen, F. H.; Jakobsen, H. J.; Ellis, P. D.; Nielsen, N. C. *J. Magn. Reson.* **1998**, *131*, 144–147.

(38) O'Dell, L. A.; Schurko, R. W. *Chem. Phys. Lett.* **2008**, *464*, 117–130.

(39) Harris, K. J.; Lupulescu, A.; Lucier, B. E. G.; Frydman, L.; Schurko, R. W. *J. Magn. Reson.* **2012**, *224*, 38–47.

(40) Harris, R. K.; Becker, E. D.; Menezes, S. M. C. D. E. *Pure Appl. Chem.* **2001**, *73*, 1795–1818.

(41) Kentgens, A. P. M. *Geoderma* **1997**, *80*, 271–306.

(42) Chapman, R. P.; Hiscock, J. R.; Gale, P. A.; Bryce, D. L. *Can. J. Chem.* **2011**, *89*, 822–834.

(43) Bryce, D. L.; Gee, M.; Wasylishen, R. E. *J. Phys. Chem. A* **2001**, *105*, 10413–10421.

(44) Hamaed, H.; Pawlowski, J. M.; Cooper, B. F. T.; Fu, R.; Eichhorn, S. H.; Schurko, R. W. *J. Am. Chem. Soc.* **2008**, *130*, 11056–11065.

(45) Chapman, R. P.; Bryce, D. L. *Phys. Chem. Chem. Phys.* **2009**, *11*, 6987–6998.

(46) Rossini, A. J.; Mills, R. W.; Briscoe, G. A.; Norton, E. L.; Geier, S. J.; Hung, I.; Zheng, S.; Autschbach, J.; Schurko, R. W. *J. Am. Chem. Soc.* **2009**, *131*, 3317–3330.

(47) Johnston, K. E.; O'Keefe, C. A.; Gauvin, R. M.; Trébosc, J.; Delevoye, L.; Amoureux, J.-P.; Popoff, N.; Taoufik, M.; Oudatchin, K.; Schurko, R. W. *Chem. Eur. J.* **2013**, *19*, 12396–12414.

(48) Perras, F. A.; Bryce, D. L. *Angew. Chem. Int. Ed. Engl.* **2012**, *51*, 4227–4230.

(49) Schurko, R. W. In *Encyclopedia of Magnetic Resonance*; John Wiley and Sons, 2012; pp. 77–94.

(50) Schurko, R. W. *Acc. Chem. Res.* **2013**, *46*, 1985–1995.

(51) O'Dell, L. A.; Rossini, A. J.; Schurko, R. W. *Chem. Phys. Lett.* **2009**, *468*, 330–335.

(52) Taylor, J. C.; Wilson, P. W. *Acta Crystallogr. Sect. B Struct. Sci.* **1974**, *30*, 1216–1220.

(53) Popoff, N.; Espinas, J.; Gouré, E.; Boyron, O.; Le Roux, E.; Basset, J.-M.; Gauvin, R. M.; De Mallmann, A.; Taoufik, M. *Macromol. Rapid Commun.* **2011**, *32*, 1921–1924.

(54) Kraus, W.; Nolze, G. PowderCell for Windows, 2000.

(55) Massiot, D.; Farnan, I.; Gautier, N.; Trumeau, D.; Trokiner, A.; Coutures, J. P. *Solid State Nucl. Magn. Reson.* **1995**, *4*, 241–248.

(56) Medek, A.; Frydman, V.; Frydman, L. *J. Phys. Chem. A* **1999**, *103*, 4830–4835.

(57) Tang, J. A.; Masuda, J. D.; Boyle, T. J.; Schurko, R. W. *ChemPhysChem* **2006**, *7*, 117–130.

(58) Eichele, K.; Wasylishen, R. E. WSolids: Solid-State NMR Spectrum Simulation Package, 2001.

(59) Perras, F. A.; Widdifield, C. M.; Bryce, D. L. *Solid State Nucl. Magn. Reson.* **2012**, *45-46*, 36–44.

(60) Clark, S. J.; Segall, M. D.; Pickard, C. J.; Hasnip, P. J.; Probert, M. I. J.; Refson, K.; Payne, M. C. *Z. Krist.* **2005**, *220*.

(61) Baerends, E. J. Z. T.; Autschbach, J. Amsterdam Density Functional.

(62) Van Lenthe, E.; Snijders, J. G.; Baerends, E. J. *J. Chem. Phys.* **1996**, *105*, 6505–6516.

(63) Hammer, B.; Hansen, L.; Nørskov, J. *Phys. Rev. B* **1999**, *59*, 7413–7421.

(64) Perdew, J.; Burke, K.; Ernzerhof, M. *Phys. Rev. Lett.* **1996**, *77*, 3865–3868.

(65) Autschbach, J.; Zheng, S.; Schurko, R. W. *Concepts Magn. Reson.* **2010**, *36A*, 84–126.

(66) Reed, A. E.; Weinhold, F. *J. Chem. Phys.* **1985**, *83*, 1736.

(67) Glendening, E. D.; Badenhoop, J. K.; Reed, A. E.; Carpenter, J. E.; Bohmann, J. A.; Morales, C. M.; Weinhold, F. NBO 5.0, 2001.

(68) Harris, R. K. *Analyst* **2006**, *131*, 351–373.

(69) Lucken, E. A. C. In *Nuclear Quadrupole Coupling Constants*; Academic Press: New York, 1969; pp. 34–45.

(70) Das, T. P.; Hahn, E. L. In *Nuclear Quadrupole Resonance Spectroscopy*; Academic Press: New York, 1958; pp. 3–7.

(71) Smith, D. K.; Landingham, R. L.; Smith, G. S.; Johnson, Q. *Acta Crystallogr. Sect. B Struct. Sci.* **1968**, *24*, 1563.

(72) Pisarev, E. A.; Semin, G. K.; Drobot, D. V.; Kuznetsov, S. I.; Bryukhova, E. V. *Zh. Neorg. Khim.* **1974**, *23*, 1171–1182.

(73) Suits, B. H. *Nuclear Quadrupolar Spectroscopy in Handbook of Applied Solid-State Spectroscopy*; Vij, D. R., Ed.; Springer: New York, 2006.

(74) Widdifield, C. M.; Chapman, R. P.; Bryce, D. L. *Annu. Reports NMR Spectrosc.* **2009**, *66*, 195.

(75) Rossini, A. J.; Hamaed, H.; Schurko, R. W. *J. Magn. Reson.* **2010**, *206*, 32–40.

(76) Hess, H.; Hartung, H. *Z. Anorg. Chem.* **1966**, *344*.

(77) Taylor, J. C.; Waugh, A. B. *Dalt. Trans.* **1980**, *10*, 2006–2009.

(78) Lucken, E. A. C. In *Nuclear Quadrupole Coupling Constants*; Academic Press: New York, 1969; pp. 120–130.

(79) Zalkin, A.; Sands, D. E. *Acta Crystallogr.* **1958**, *11*, 615–619.

(80) Rabe, S.; Mueller, U. *Z. Krist. - New Cryst. Struc.* **2000**, *215*, 1–2.

(81) Semin, G. K.; Kuznetsov, S. I.; Alimov, I. M.; Khotsianova, T. L.; Bryukhova, E. V.; Nisselson, L. A.; Tretyakova, K. V. *Inorg. Chim. Acta* **1974**, *13*, 181.

(82) Lucier, B. E. G.; Tang, J. A.; Schurko, R. W.; Bowmaker, G. A.; Healy, P. C.; Hanna, J. V. *J. Phys. Chem. C* **2010**, *114*, 7949–7962.

(83) Dye, J. L.; Ellaboudy, A. S.; Kim, J. *Solid State NMR of Quadrupolar Nuclei*; Marcel Dekker, Inc.: New York, 1991.

**Scheme 1**. Schematic representation of **(A)** tungsten(VI) chloride ($WCl_6$), **(B)** tetrachlorotungsten(VI) oxide ($WOCl_4$) and tetrachloromolybdenum(VI) oxide ($MoOCl_4$) **(C)** niobium(V) chloride ($NbCl_5$) and tantalum(V) chloride ($TaCl_5$) and **(D)** the different chlorine bonding environments in the bridging pentahalide species. Bridging chlorine atoms ($Cl_{br}$) are shown in blue, terminal-axial ($Cl_{ax}$) in green and terminal-equatorial ($Cl_{eq}$) in orange.

**Figure 1**. Comparison between the experimental and calculated values of **(A)** $C_Q$ and **(B)** $\eta_Q$ for all sites within the complexes studied. All calculated values were obtained from $^{35}Cl$ EFG tensor calculations completed on geometry optimized structures using CASTEP. The values of both $C_Q$ and $\eta_Q$ for the pseudo-bridging chlorine sites in $MoOCl_4$ were omitted due to poor correlation between experiment and calculation.

**Figure 2**: Static $^{35}Cl$ SSNMR spectrum acquired using frequency-stepped WURST-CPMG for **(A)** α-$WCl_6$ at 21.1 T and **(B)** β-$WCl_6$ at 9.4 T with corresponding analytical simulations shown in red. **(C)** Hahn-echo experiments conducted on β-$WCl_6$ at (i) the high and (ii) the low frequency discontinuities. $^{35}Cl$ NQR spectra for **(D)** α-$WCl_6$ and **(E)** β-$WCl_6$. The NQR frequencies ($\nu_Q^{NQR}$) for each of the sites are shown in the figure. The spectra were acquired with a transmitter frequency of 10.52 MHz.

**Figure 3**. Theoretical $^{35}Cl$ EFG tensor orientations in the molecular frames for **(A)** α-$WCl_6$ and **(B)** β-$WCl_6$, **(C)** $WOCl_4$, **(D)** $MoOCl_4$ with (i) the pseudo-bridging chlorine sites (Cl1), (ii) the terminal chloride sites opposite the bridging sites (Cl2) and (iii) the

terminal chlorine sites adjacent to the bridging chlorine sites (Cl3 and Cl4) and **(E)** $NbCl_5$ with (i) $Cl_{br}$, (ii) $Cl_{eq}$ and (iii) $Cl_{ax}$. All pictured orientations were determined from $^{35}Cl$ EFG tensor calculations completed on geometry-optimized models using CASTEP.

**Figure 4**. Static $^{35}Cl$ SSNMR spectra acquired at 21.1 T for **(A)** $WoCl_4$ and **(B)** $MoOCl_4$. Analytical simulations representative of the entire powder patterns are shown in red while individual sites are shown in blue (Cl1), green (Cl2), black (Cl3) and orange (Cl4).

**Figure 5**. Static $^{35}Cl$ SSNMR spectra acquired at 21.1 T for **(A)** $NbCl_5$ and **(B)** $TaCl_5$. Corresponding analytical simulations representative of the entire powder patterns are shown in red and simulations of the individual sites are shown in blue ($Cl_{br}$), green ($Cl_{ax}$) and orange ($Cl_{eq}$).

**Figure 6**. $T_2$ relaxation time constants and corresponding CPMG echo trains from experiments on α-$WCl_6$ at **(A)** the high-frequency, **(B)** central and **(C)** low-frequency discontinuities.

**Figure 7. (A)** Atom numbering of the $Nb_2Cl_{10}$ unit used in the LMO analysis. **(B)** Isosurface representations of the LMOs (**1**) σ($Cl_{ax}$-Nb), (**2**) σ LP $Cl_{ax}$, (**3**) $\pi_x$ LP $Cl_{ax}$, (**4**) $\pi_y$ LP $Cl_{ax}$, (**5**) σ($Cl_{eq}$-Nb), (**6**) σ LP $Cl_{eq}$, (**7**) π($Cl_{eq}$-Nb), (**8**) $\pi_z$ LP $Cl_{eq}$, (**9**) $\pi_x$ LP $Cl_{br}$ (with some μ-bonding character), (**10**) μ(Nb-Cl-Nb), (**11**) σ LP $Cl_{br}$ and (**12**) $\pi_z$ LP $Cl_{br}$.

**Figure 8**. Graphical representations (polar plots) of $^{35}$Cl EFG tensors of $NbCl_5$ for **(A)** $Cl_{ax}$, **(B)** $Cl_{eq}$ and **(C)** $Cl_{br}$ environments. The blue colour indicates a positive EFG while orange indicates a negative EFG. The $V_{33}$ values are +0.71, +0.81 and −1.32 a.u., for (**A**) – (**C)** respectively.

**Figure 9.** Static $^{35}$Cl SSNMR spectrum acquired using the WURST-CPMG pulse sequence at 18.8 T for silica-supported $WCl_6$ with corresponding analytical simulation shown in red.

**Table 1**. $^{35}$Cl NMR parameters obtained from spectra acquired at 21.1 T.

| Sample | Site | $\lvert C_Q \rvert$[a] | $\eta_Q$[b] | $\delta_{iso}$[c] | $\Omega$[d] | $\kappa$[e] | $\alpha$[f] | $\beta$ | $\gamma$ |
|---|---|---|---|---|---|---|---|---|---|
| **$\alpha$-$WCl_6$** | 1 | 21.00(10) | 0.029(5) | 800(40) | 200(100) | 1.0(2) | 0(10) | 0(10) | 0(10) |
| **$\beta$-$WCl_6$** | 1 | 21.00(10) | 0.029(5) | 800(40) | 200(100) | 1.0(2) | 0(10) | 0(10) | 0(10) |
| **$WOCl_4$** | 1 | 26.05(10) | 0.115(5) | 620(50) | 550(150) | -1.0(4) | 50(5) | 15(10) | 50(5) |
| **$MoOCl_4$** | 1 | 30.50(10) | 0.585(10) | 650(50) | 800(100) | 1.0(2) | 0(5) | 90(5) | 0(10) |
| | 2 | 25.30(10) | 0.510(5) | 950(100) | 800(150) | 1.0(2) | 0(5) | 90(5) | 90(5) |
| | 3 | 25.00(10) | 0.500(5) | 800(50) | 300(100) | 1.0(3) | 0(10) | 90(10) | 0(10) |
| | 4 | 23.30(5) | 0.540(20) | 730(30) | 235(50) | 0.0(5) | 0(20) | 0(10) | 0(20) |
| **$NbCl_5$** | 1 | 25.30(5) | 0.385(10) | 250(150) | 460(300) | 1.0(2) | 90(30) | 0(10) | 90(30) |
| | 2 | 15.00(8) | 0.081(7) | 850(50) | 200(200) | 0.0(5) | 0(20) | 0(5) | 0(30) |
| | 3 | 14.70(9) | 0.655(5) | 990(40) | 300(200) | 0.0(3) | 45(15) | 0(20) | 45(15) |
| **$TaCl_5$** | 1 | 25.70(8) | 0.430(10) | 260(100) | 250(200) | 1.0(5) | 90(30) | 0(10) | 90(30) |
| | 2 | 15.65(15) | 0.043(6) | 640(50) | 300(100) | 1.0(3) | 0(30) | 0(5) | 0(30) |
| | 3 | 16.70(30) | 0.480(20) | 900(40) | 700(50) | -1.0(3) | 0(30) | 90(5) | 0(30) |
| **$WCl_6$-$SiO_2$** | 1 | 25.98(5) | 0.11(1) | 450(30) | 300(100) | -1.0(5) | 50(10) | 15(5) | 50(10) |

[a] $C_Q = eQV_{33}/h$, [b] $\eta_Q = (V_{11} - V_{22})/V_{33}$, [c] $\delta_{iso} = (\delta_{11} + \delta_{22} + \delta_{33})/3$, [d] $\Omega = \delta_{11} - \delta_{33}$, [e] $\kappa = 3(\delta_{22} - \delta_{iso})/\Omega$ , [f]the Euler angles, $\alpha$, $\beta$ and $\gamma$, define the relative orientations of the EFG and CS tensors. The "ZYZ" convention for rotation is used herein, as described by Dye *et al.*,[83] and as implemented in the WSolids[58] software package.

**Table 2.** Experimental and calculated (using CASTEP) $^{35}$Cl EFG tensor parameters and comparison of predicted NQR frequencies obtained from $^{35}$Cl SSNMR data to those reported in literature. Calculation of the NMR parameters was completed both prior to and post geometry optimization of the structure.

| | | Experimental | | Calculated | | | | | |
|---|---|---|---|---|---|---|---|---|---|
| | | | | pre-geometry optimization | | post-geometry optimization | | | |
| Complex | Site | $\lvert C_Q \rvert$ (MHz) | $\eta_Q$ | $C_Q$ (MHz) | $\eta_Q$ | $C_Q$ (MHz) | $\eta_Q$ | Predicted[a] $\nu_Q^{NQR}$ (MHz) | Reported[10, 21] $\nu_Q^{NQR}$ (MHz) |
| **α-$WCl_6$** | 1 | 21.00 | 0.029 | −15.62 | 0.06 | −18.58 | 0.05 | 10.501 | 10.520 |
| **β-$WCl_6$** | 1 | 21.00 | 0.029 | −16.39 | 0.01 | −18.65 | 0.07 | 10.501 | 10.520 |
| | 2 | | | −29.83 | 0.10 | −18.60 | 0.07 | | 10.525 |
| | 3 | | | −8.001 | 0.01 | −18.73 | 0.07 | | 10.576 |
| **$WOCl_4$** | 1 | 26.05 | 0.115 | −22.06 | 0.08 | −23.39 | 0.14 | 13.054 | 13.076 |
| **$MoOCl_4$** | 1 | 30.50 | 0.585 | −30.66 | 0.10 | −24.07 | 0.31 | 16.096 | 15.658 |
| | 2 | 25.30 | 0.510 | −15.64 | 0.94 | −23.09 | 0.41 | 13.187 | 13.088 |
| | 3 | 25.00 | 0.500 | −23.39 | 0.56 | −25.50 | 0.44 | 13.010 | 12.904 |
| | 4 | 23.30 | 0.540 | −26.44 | 0.33 | −23.17 | 0.41 | 12.203 | 12.757 |
| **$NbCl_5$** | 1 | 14.70 | 0.655 | −12.10 | 0.81 | −12.72 | 0.77 | 7.858 | 7.612 |
| | 2 | 15.00 | 0.081 | −11.92 | 0.14 | −12.31 | 0.09 | 7.508 | 7.219 |
| | 3 | | | −12.08 | 0.85 | −12.95 | 0.77 | | 7.365 |
| | 4 | | | −11.76 | 0.10 | −12.28 | 0.08 | | 7.721 |
| | 5 | | | −11.90 | 0.84 | −12.80 | 0.77 | | |
| | 6 | | | −11.70 | 0.08 | −12.35 | 0.07 | | |
| | 7 | 25.30 | 0.385 | 24.29 | 0.28 | 23.90 | 0.27 | 12.959 | 13.058 |
| | 8 | | | 23.89 | 0.32 | 23.97 | 0.27 | | |
| | 9 | | | 23.69 | 0.33 | 23.79 | 0.28 | | |
| **$TaCl_5$** | 1 | 16.70 | 0.48 | −13.58 | 0.71 | −15.47 | 0.63 | 8.665 | 8.141 |
| | 2 | 15.65 | 0.043 | −14.35 | 0.09 | −15.29 | 0.06 | 7.827 | 7.598 |
| | 3 | | | −13.88 | 0.72 | −15.63 | 0.63 | | 8.261 |
| | 4 | | | −13.99 | 0.08 | −15.34 | 0.06 | | 7.641 |
| | 5 | | | −13.66 | 0.74 | −15.64 | 0.63 | | 8.231 |
| | 6 | | | −13.82 | 0.07 | −15.38 | 0.05 | | 7.663 |
| | 7 | 25.70 | 0.430 | 25.38 | 0.34 | 25.93 | 0.30 | 13.240 | 13.334 |
| | 8 | | | 25.52 | 0.32 | 25.98 | 0.31 | | 13.356 |
| | 9 | | | 25.54 | 0.32 | 25.89 | 0.31 | | 13.377 |

[a] The NQR frequencies were calculated from NMR parameters obtained from solid-state $^{35}$Cl SSNMR spectra using $\nu_Q^{NQR} = (C_Q/2)\sqrt{(1+(\eta_Q)^2/3)}$

**Table 3.** LMO contributions to the $^{35}$Cl EFG tensors of the various chlorine environments in $NbCl_5$.

| MO # | Orbital Type[a] | NLMO Composition[b] | Contributions to $V_{11}$[c] | | | Contributions to $V_{22}$[c] | | | Contributions to $V_{33}$[c] | | |
|---|---|---|---|---|---|---|---|---|---|---|---|
| | | | $Cl_{ax}$ | $Cl_{eq}$ | $Cl_{br}$ | $Cl_{ax}$ | $Cl_{eq}$ | $Cl_{br}$ | $Cl_{ax}$ | $Cl_{eq}$ | $Cl_{br}$ |
| **1** | σ($Cl_{ax}$-Nb) | 82 Cl (26 *s*, 74 *p*) 15 Nb (18 *s*, 1 *p*, 81 *d*) | 2.81 | 0.01 | 0.00 | 2.85 | –0.01 | 0.01 | –5.66 | 0.00 | –0.01 |
| **2** | σ LP $Cl_{ax}$ | 99 Cl (73 *s*, 27 *p*) | 0.88 | 0.00 | 0.00 | 1.14 | –0.01 | 0.01 | –2.02 | 0.01 | –0.01 |
| **3** | $\pi_x$ LP $Cl_{ax}$ | 87 Cl (1 *s*, 99 *p*) 11 Nb (1 *s*, 1 *p*, 98 *d*) | –4.99 | 0.00 | 0.00 | 1.08 | –0.01 | 0.01 | 3.91 | 0.00 | –0.01 |
| **4** | $\pi_y$ LP $Cl_{ax}$ | 87 Cl (100 *p*) 11 Nb (1 *p*, 99 *d*) | 1.03 | 0.01 | 0.01 | –5.31 | –0.01 | 0.00 | 4.28 | 0.01 | –0.01 |
| **5** | σ($Cl_{eq}$-Nb) | 78 Cl (25 *s*, 75 *p*) 22 Nb (20 *s*, 1 *p*, 79 *d*) | –0.01 | 1.13 | 0.01 | 0.01 | 2.80 | –0.01 | 0.00 | –3.93 | 0.00 |
| **6** | σ LP $Cl_{eq}$ | 99 Cl (74 *s*, 26 *p*, 0.02 *d*) | –0.01 | 0.96 | 0.01 | 0.00 | 1.17 | –0.01 | 0.01 | –2.13 | 0.00 |
| **7** | π($Cl_{eq}$-Nb) | - | –0.01 | –6.43 | 0.01 | 0.00 | 4.06 | –0.02 | 0.00 | 2.38 | 0.01 |
| **8** | $\pi_z$ LP $Cl_{eq}$ | 89 Cl (100 *p*) 8 Nb (20 *s*, 1 *p*, 79 *d*) | –0.16 | 4.47 | 0.01 | 0.07 | –8.93 | –0.01 | 0.09 | 4.46 | 0.00 |
| **9** | $\pi_x$ LP $Cl_{br}$ (μ) | 86 Cl (100 *p*) 6 Nb (18 *s*, 3 *p*, 79 *d*) 5 Nb (19 *s*, 3 *p*, 78 *d*) | 0.01 | –0.02 | 3.88 | –0.01 | 0.01 | –7.77 | 0.00 | 0.01 | 3.89 |
| **10** | μ(Nb-Cl-Nb) | 84 Cl (30 *s*, 70 *p*) 6 Nb (15 *s*, 1 *p*, 83 *d*) 6 Nb (16 *s*, 1 *p*, 83 *d*) | 0.00 | –0.02 | –5.39 | 0.00 | 0.01 | 2.68 | 0.00 | 0.01 | 2.71 |
| **11** | σ LP $Cl_{br}$ | 98 Cl (70 *s*, 30 *p*) 1 Nb (9 *s*, 1 *p*, 89 *d*) | 0.00 | –0.02 | –2.66 | –0.01 | 0.01 | 1.33 | 0.01 | 0.01 | 1.32 |
| **12** | $\pi_z$ LP $Cl_{br}$ | 94 Cl (100 *p*) | 0.03 | –0.01 | 4.59 | –0.04 | 0.00 | 4.60 | 0.01 | 0.01 | –9.19 |
| - | π($Cl_{ax}$-Nb) | - | –0.01 | –0.01 | 0.01 | –0.01 | –0.01 | 0.01 | 0.02 | 0.02 | –0.02 |
| - | π LP Cls | - | 0.02 | –0.24 | –0.11 | –0.17 | 0.18 | 0.10 | 0.15 | 0.06 | 0.02 |
| - | σ LP Cls | - | –0.02 | –0.03 | –0.01 | –0.03 | –0.03 | 0.04 | 0.05 | 0.05 | –0.03 |
| - | σ(Cls-Nb) | - | 0.00 | 0.00 | 0.03 | –0.02 | –0.03 | –0.01 | 0.01 | 0.03 | –0.02 |
| - | Core $Cl_{ax}$ | 100 Cl | –0.03 | 0.02 | 0.02 | –0.04 | –0.04 | 0.04 | 0.06 | 0.03 | –0.05 |
| - | Core $Cl_{eq}$ | 100 Cl | –0.05 | –0.01 | 0.04 | 0.01 | –0.06 | –0.04 | 0.04 | 0.08 | 0.01 |
| - | Core $Cl_{br}$ | 100 Cl | 0.02 | –0.03 | 0.05 | –0.03 | 0.01 | 0.11 | 0.01 | 0.02 | –0.16 |
| - | Core Cls | 100 Cl | –0.11 | –0.13 | –0.01 | –0.13 | –0.13 | 0.18 | 0.23 | 0.26 | –0.17 |
| - | Core Nb | 100 Nb | 0.24 | 0.26 | –0.07 | 0.28 | 0.30 | –0.32 | –0.52 | –0.57 | 0.40 |
| | | Total calculated | –0.35 | –0.09 | 0.40 | –0.35 | –0.72 | 0.92 | 0.71 | 0.81 | –1.32 |
| | | Experimental | - | - | - | - | - | - | 0.74 | 0.75 | 1.32 |

[a]"Core" refers to non-bonding orbitals in the subshells below the valence shell, π LP denotes chlorine lone pairs which may participate in π-bonding, σ LP are lone pairs of σ-symmetry with respect to the Cl-Nb axis, and π, σ and μ represent orbitals with significant covalent nature. [b]The composition of an LMO with each number signifying percentages. The contributions from each atom as well as the atomic orbital character for selected LMOs are shown. [c]The contributions of each orbital towards $V_{11}$, $V_{22}$ and $V_{33}$ are given in a.u.

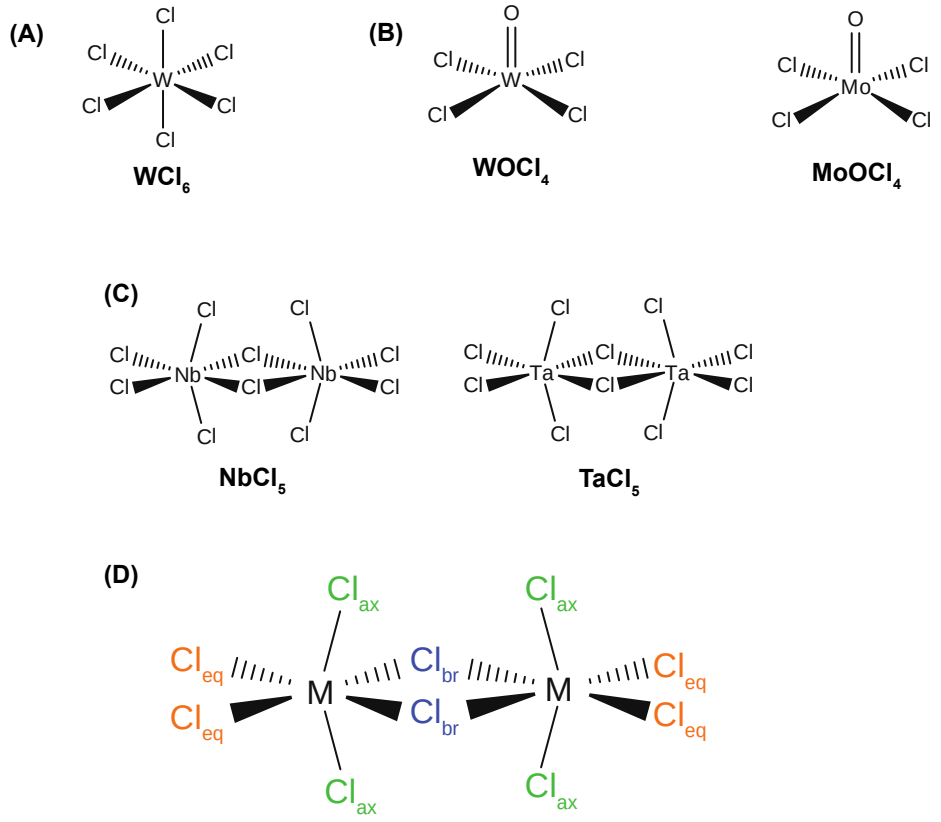


**Scheme 1.** Schematic representations of **(A)** tungsten(VI) chloride ($WCl_6$), **(B)** tetrachlorotungsten(VI) oxide ($WOCl_4$) and tetrachloromolybdenum(VI) oxide ($MoOCl_4$), **(C)** niobium(V) chloride ($NbCl_5$) and tantalum(V) chloride ($TaCl_5$) and **(D)** the different chlorine bonding environments in the bridging pentahalide species. Bridging chlorine atoms ($Cl_{br}$) are shown in blue, terminal-axial ($Cl_{ax}$) in green and terminalequatorial ($Cl_{eq}$) in orange.

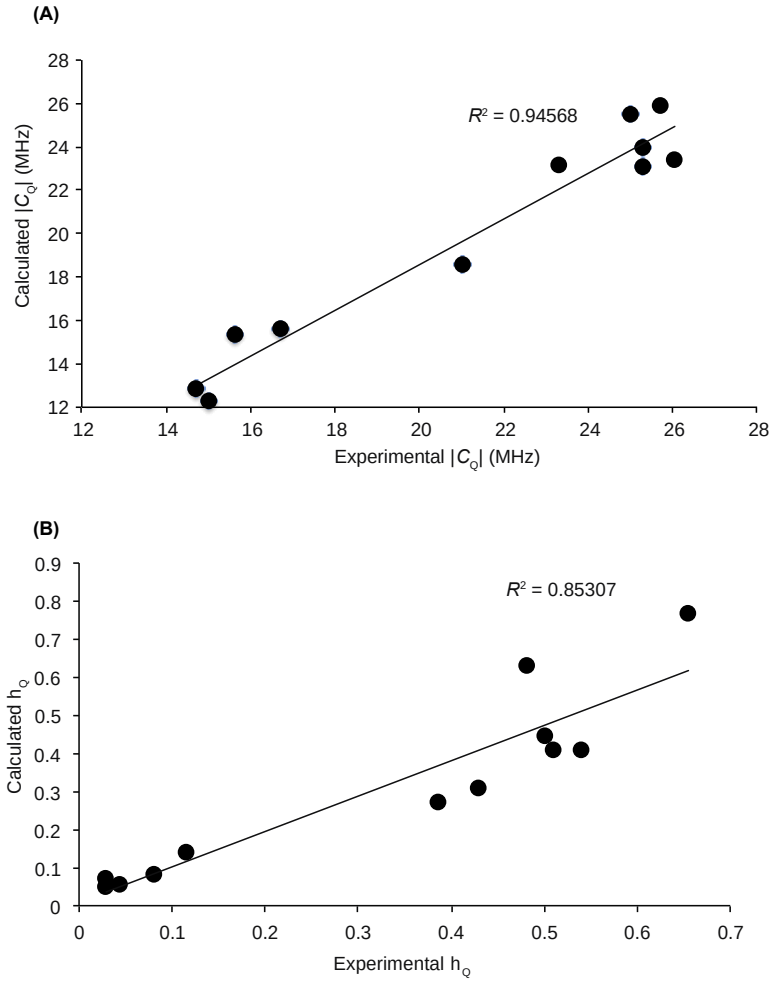


**Figure 1.** Comparison between the experimental and calculated values of **(A)** $C_Q$ and **(B)** $h_Q$ for all sites within the complexes studied. All calculated values were obtained from $^{35}$Cl EFG tensor calculations completed on geometry optimized structures using CASTEP. The values of both $C_Q$ and $h_Q$ for the pseudo-bridging chlorine sites in $MoOCl_4$ were omitted due to poor correlation between experiment and calculation.

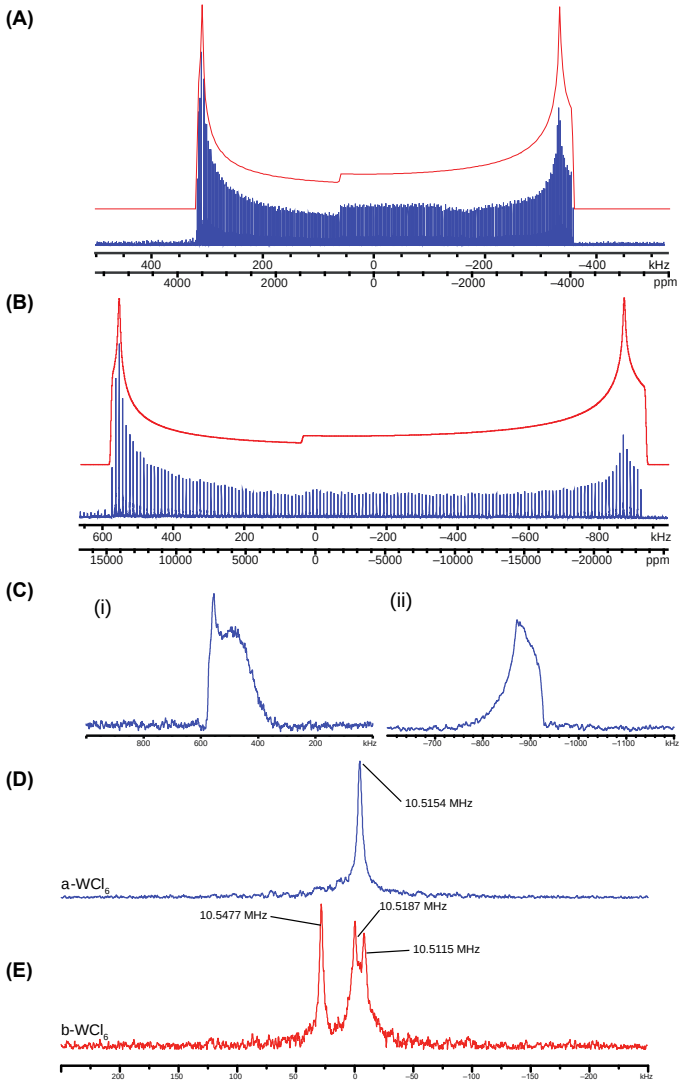


**Figure 2.** Static $^{35}$Cl SSNMR spectrum acquired using frequency-stepped WURST-CPMG for (**A**) a-$WCl_6$ at 21.1 T and (**B**) b-$WCl_6$ at 9.4 T with corresponding analytical simulations shown in red. (**C**) Hahn-echo experiments conducted on b-$WCl_6$ at (i) the high and (ii) the low frequency discontinuities. $^{35}$Cl NQR spectra for (**D**) a-$WCl_6$ and (**E**) b-$WCl_6$. The NQR frequencies ($n_Q^{NQR}$) for each of the sites are shown in the figure. The spectra were acquired with a transmitter frequency of 10.52 MHz.

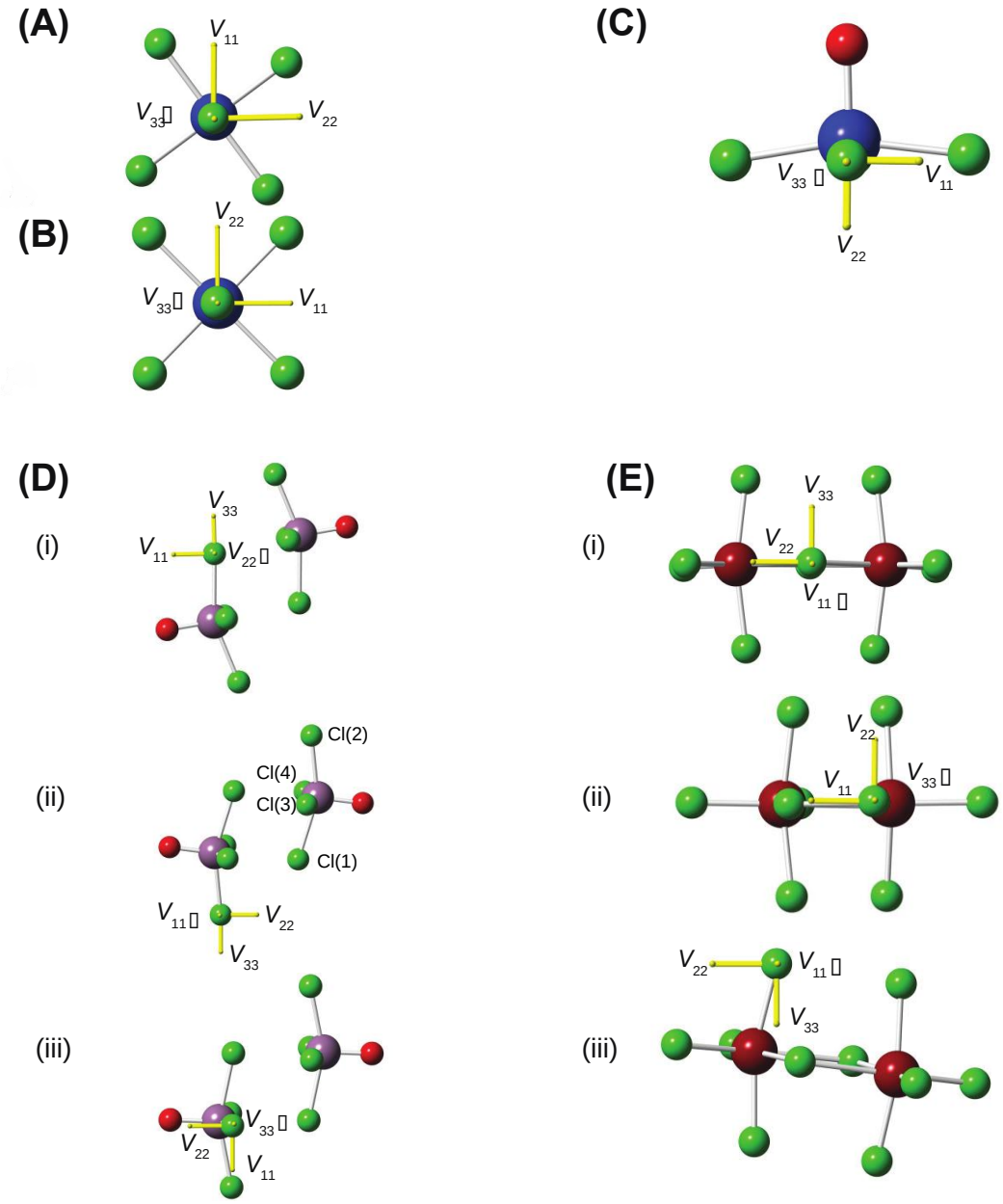


**Figure 3.** Theoretical $^{35}Cl$ EFG tensor orientation in the molecular frames for **(A)** a-$WCl_6$ and **(B)** b-$WCl_6$, **(C)** $WOCl_4$, **(D)** $MoOCl_4$ with (i) the pseudo-bridging chlorine sites (Cl1), (ii) the terminal chlorine sites opposite the pseudo-bridging sites (Cl2) and (iii) the terminal chlorine sites adjacent to the pseudo-bridging chlorine sites (Cl3 and Cl4) and **(E)** $NbCl_5$ with (i) $Cl_{br}$, (ii) $Cl_{eq}$ and (iii) $Cl_{ax}$. All pictured orientations were determined from $^{35}Cl$ EFG tensor calculations completed on geometry - optimized models using CASTEP.

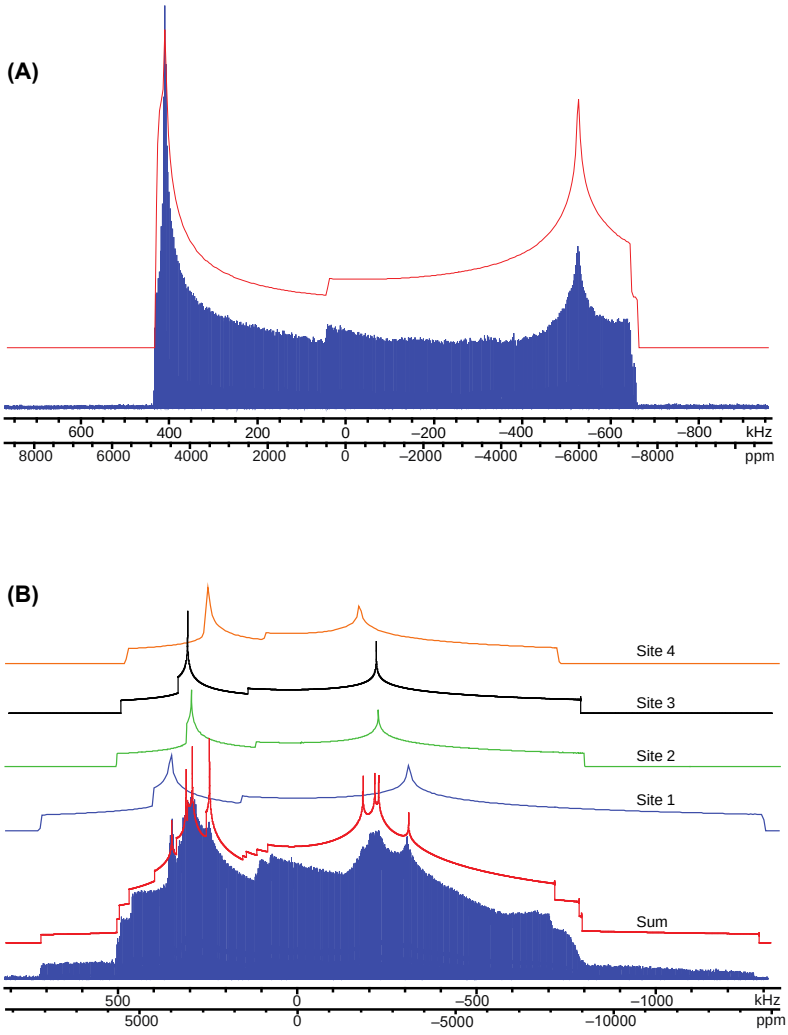


**Figure 4.** Static $^{35}$Cl SSNMR spectra acquired at 21.1 T for **(A)** $WOCl_4$ and **(B)** $MoOCl_4$. Analytical simulations representative of the entire powder patterns are shown in red, while individual sites are shown in blue (Cl1), green (Cl2), black (Cl3) and orange (Cl4).

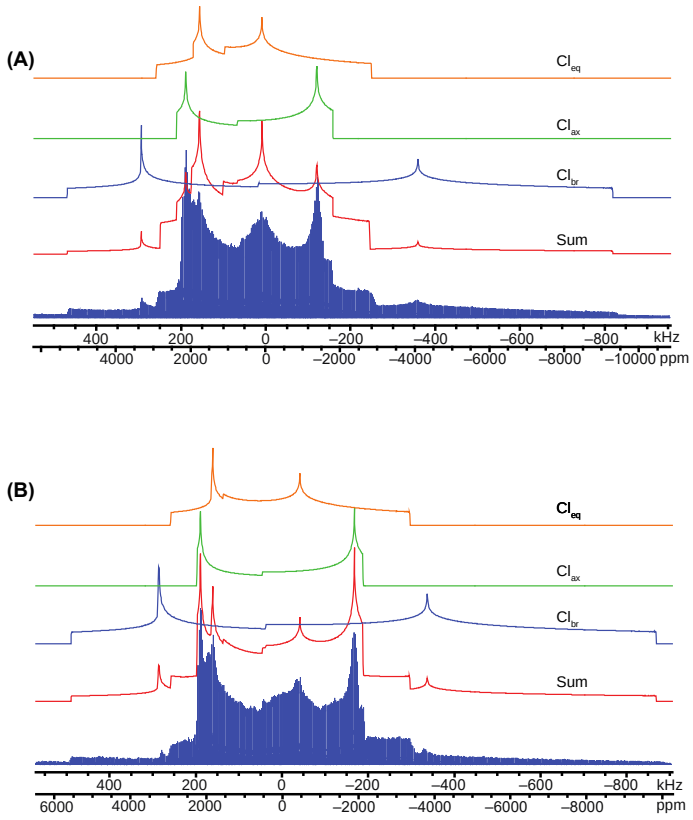


**Figure 5.** Static $^{35}Cl$ SSNMR spectra acquired at 21.1 T for **(A)** $NbCl_5$ and **(B)** $TaCl_5$. Corresponding analytical simulations representative of the entire powder patterns are shown in red and simulations of the individual sites are shown in blue ($Cl_{br}$), green ($Cl_{ax}$) and orange ($Cl_{eq}$).

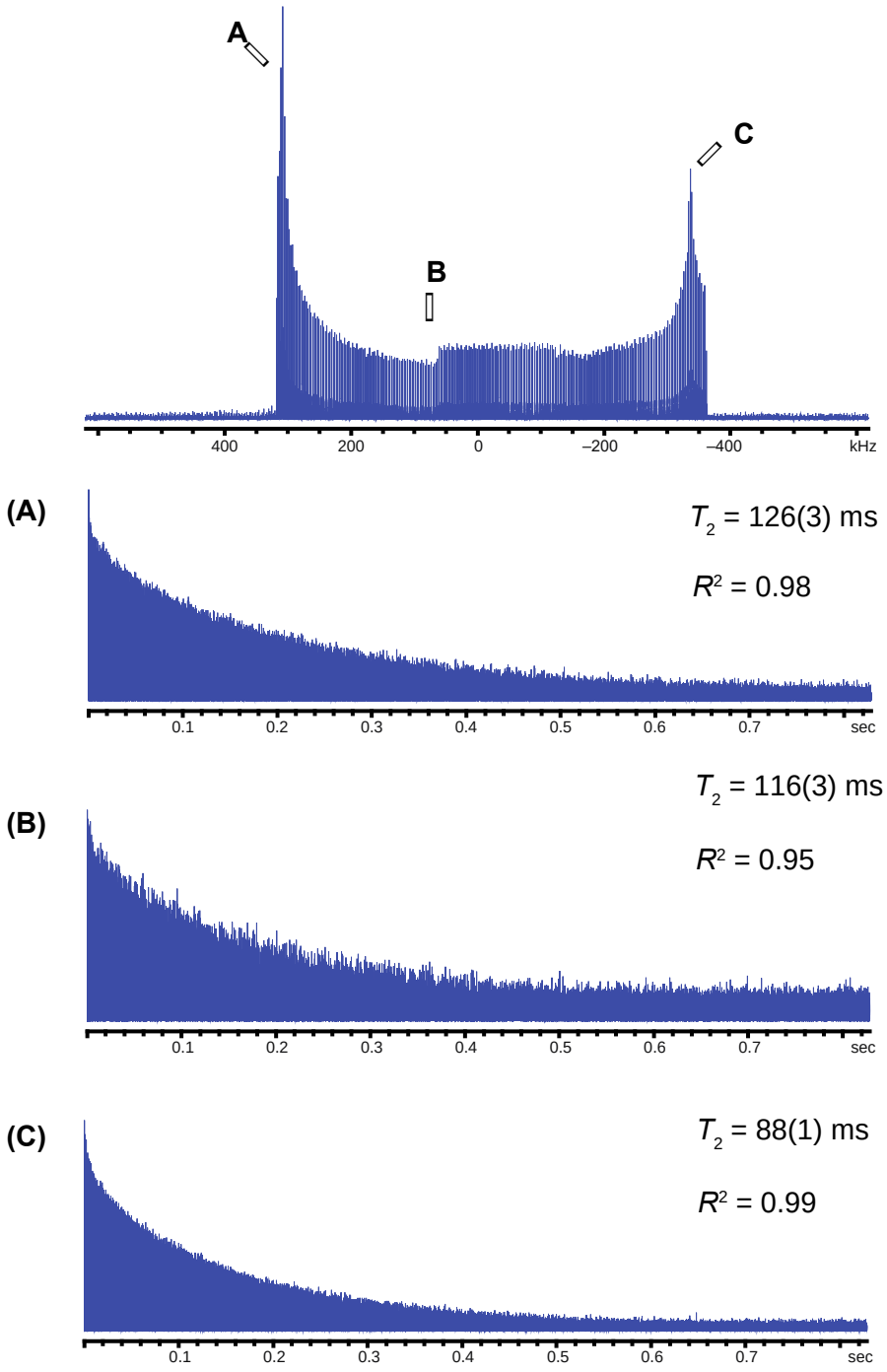


**Figure 6.** $T_2$ relaxation time constants and correspon ding CPMG echo trains from experiments on a-$WCl_6$ at **(A)** the high-frequency, **(B)** central and **(C)** low-frequency discontinuities.

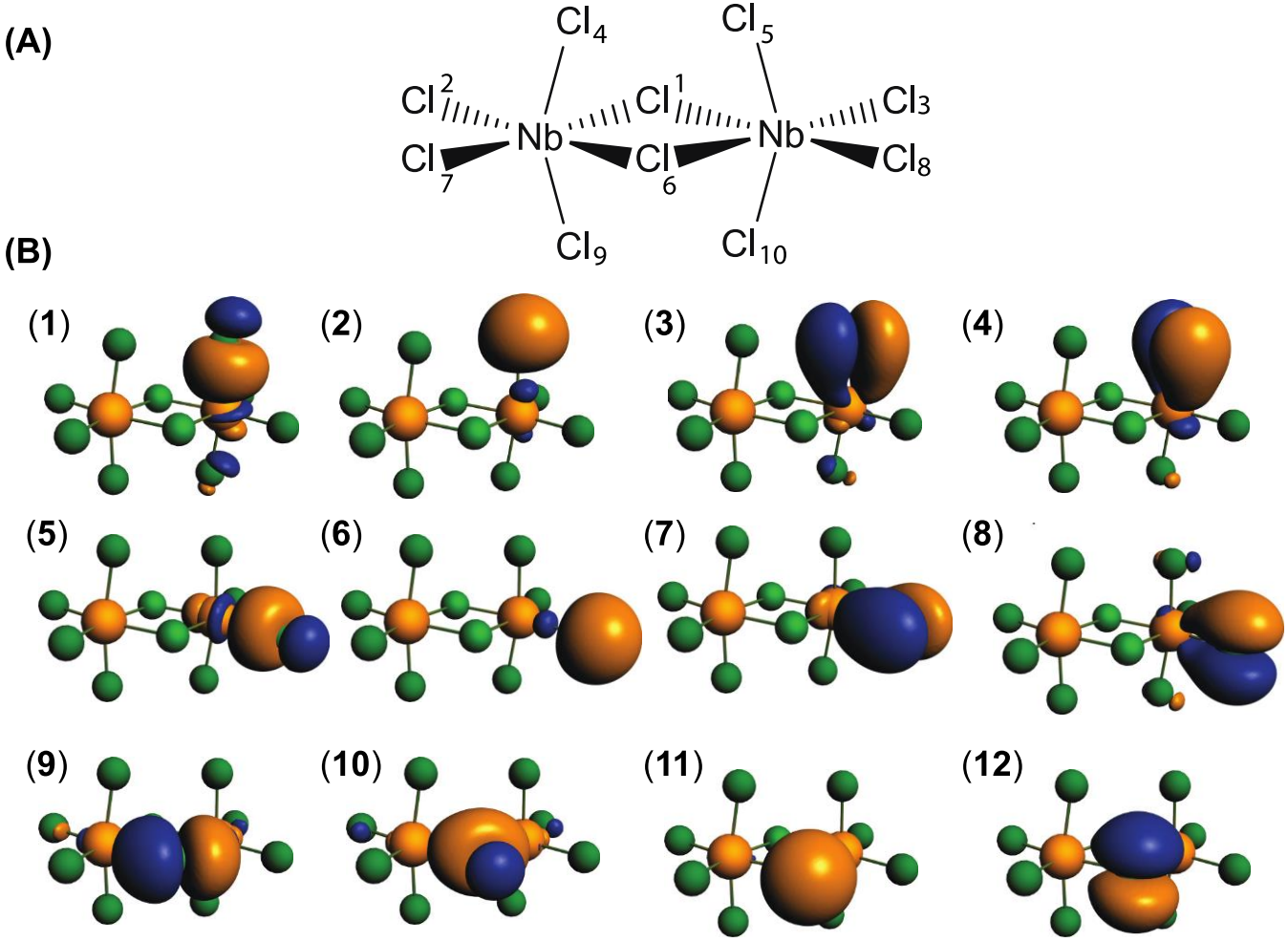


**Figure 7. (A)** Atom numbering of the $Nb_2Cl_{10}$ unit used in the LMO analysis. **(B)** Isosurface representations of the LMOs (**1**) σ($Cl_{ax}$-Nb), (**2**) σ LP $Cl_{ax}$, (**3**) $\pi_x$ LP $Cl_{ax}$, (**4**) $\pi_y$ LP $Cl_{ax}$, (**5**) σ($Cl_{eq}$-Nb), (**6**) σ LP $Cl_{eq}$, (**7**) π($Cl_{eq}$-Nb), (**8**) $\pi_z$ LP $Cl_{eq}$, (**9**) $\pi_x$ LP $Cl_{br}$ (with some μ-bonding character), (**10**) μ(Nb-Cl-Nb), (**11**) σ LP $Cl_{br}$ and (**12**) $\pi_z$ LP $Cl_{br}$.

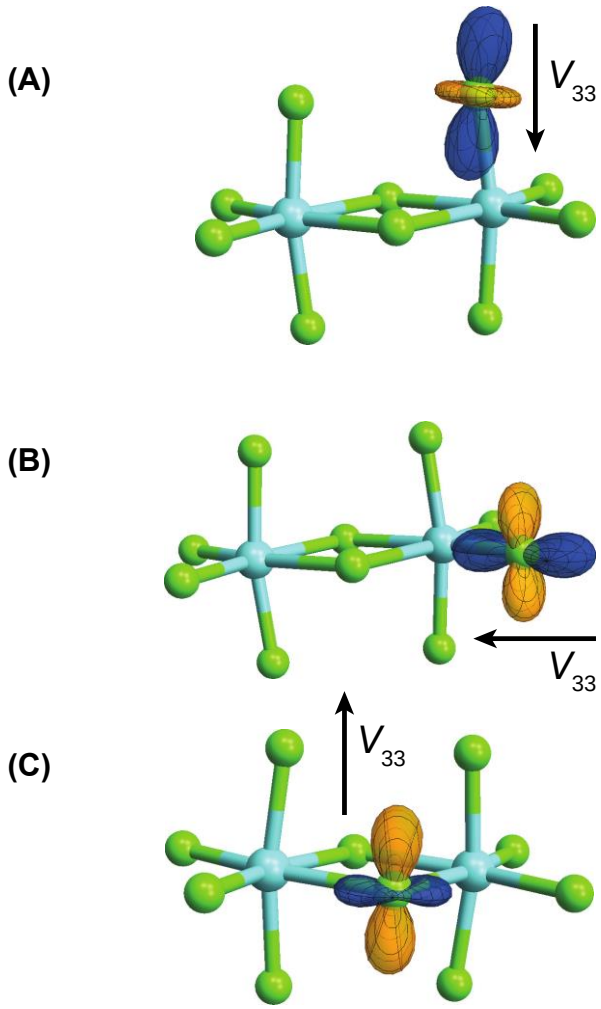


**Figure 8.** Graphical representations (polar plots) of $^{35}$Cl EFG tensors of $NbCl_5$ for **(A)** $Cl_{ax}$, **(B)** $Cl_{eq}$ and **(C)** $Cl_{br}$ environments. The blue colour indicates a positive EFG while orange indicates a negative EFG. The values of $V_{33}$ are +0.71, +0.81 and –1.32 a.u., for **(A)** - **(C)** respectively.

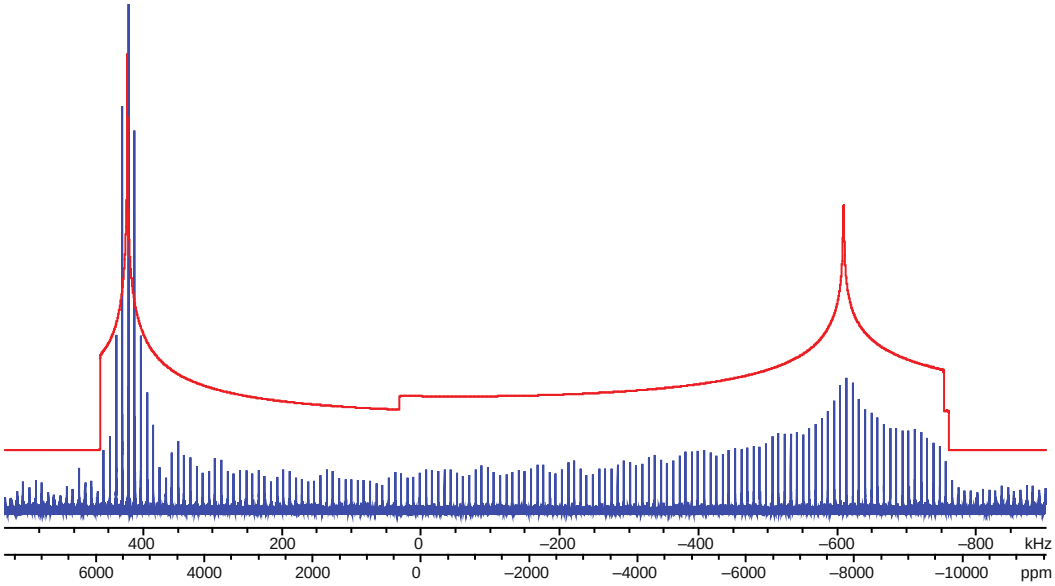


**Figure 9.** Static $^{35}$Cl SSNMR spectrum acquired using the WURST-CPMG pulse sequence at 18.8 T for silica-supported $WCl_6$ with corresponding analytical simulation shown in red.

**Table of Contents Synopsis**

$^{35}$Cl SSNMR, in tandem with $^{35}$Cl NQR and DFT calculations, was used to characterize chlorine ligands in a series of transition-metal complexes exhibiting structural motifs common to organometallic catalysts. The differentiation of the various chlorine environments was possible and insight into the origins of the $^{35}$Cl EFG tensor parameters was provided. The applicability of $^{35}$Cl SSNMR to the study of surface-supported transition-metal complexes was demonstrated, validating the use of this technique to the characterization of heterogeneous catalysts.